

Halo and Subhalo Demographics with Planck Cosmological Parameters: Bolshoi-Planck and MultiDark-Planck Simulations

Aldo Rodríguez-Puebla^{1*}, Peter Behroozi^{2,3}, Joel Primack⁴, Anatoly Klypin⁵,
Christoph Lee⁴, Doug Hellinger⁴

¹*Department of Astronomy and Astrophysics, University of California, Santa Cruz, CA 95064, USA*

²*Astronomy and Physics Departments and Theoretical Astrophysics Center, University of California, Berkeley, Berkeley CA 94720, USA*

³*Hubble Fellow*

⁴*Physics Department, University of California, Santa Cruz, CA 95064, USA*

⁵*Department of Astronomy, New Mexico State University, Las Cruces, NM 88001, USA*

Released 2016 Xxxxx XX

ABSTRACT

We report and provide fitting functions for the abundance of dark matter halos and subhalos as a function of mass, circular velocity, and redshift from the new Bolshoi-Planck and MultiDark-Planck Λ CDM cosmological simulations, based on the Planck cosmological parameters. We also report the halo mass accretion rates, which may be connected with galaxy star formation rates. We show that the higher cosmological matter density of the Planck parameters compared with the WMAP parameters leads to higher abundance of massive halos at high redshifts. We find that the median halo spin parameter $\lambda_B = J(2M_{\text{vir}}R_{\text{vir}}V_{\text{vir}})^{-1}$ is nearly independent of redshift, leading to predicted evolution of galaxy sizes that is consistent with observations, while the significant decrease with redshift in median $\lambda_P = J|E|^{-1/2}G^{-1}M^{-5/2}$ predicts more decrease in galaxy sizes than is observed. Using the Tully-Fisher and Faber-Jackson relations between galaxy velocity and mass, we show that a simple model of how galaxy velocity is related to halo maximum circular velocity leads to increasing overprediction of cosmic stellar mass density as redshift increases beyond redshifts $z \sim 1$, implying that such velocity-mass relations must change at redshifts $z \gtrsim 1$. By making a realistic model of how observed galaxy velocities are related to halo circular velocity, we show that recent optical and radio observations of the abundance of galaxies are in good agreement with our Λ CDM simulations. Our halo demographics are based on updated versions of the ROCKSTAR and CONSISTENT TREES codes, and this paper includes appendices explaining all of their outputs. This paper is an introduction to a series of related papers presenting other analyses of the Bolshoi-Planck and MultiDark-Planck simulations.

Key words: Cosmology: Large Scale Structure - Dark Matter - Galaxies: Halos - Methods: Numerical

1 INTRODUCTION

In the Λ CDM standard modern theory of structure formation in the universe, galaxies populate dark matter halos and subhalos. The demographics of these halos as a function of redshift are thus an important input to the prediction of the properties and distribution of galaxies. A number of large cosmological simulations have

now been run (see e.g. Kuhlen, Vogelsberger & Angulo 2012), although many cover large volumes but with resolution too low to identify all dark matter halos that host most galaxies. The mass resolution required to do this is $\lesssim 10^8 h^{-1} M_\odot$, and the force resolution should be $\lesssim 1 h^{-1}$ kpc. High-resolution cosmological dark matter simulations that are particularly useful for studying galaxy hosts include the Millennium simulations (Springel et al. 2005; Boylan-Kolchin et al. 2009; Angulo et al. 2012), Bolshoi (Klypin, Trujillo-Gomez & Primack 2011),

* rodriguez.puebla@gmail.com

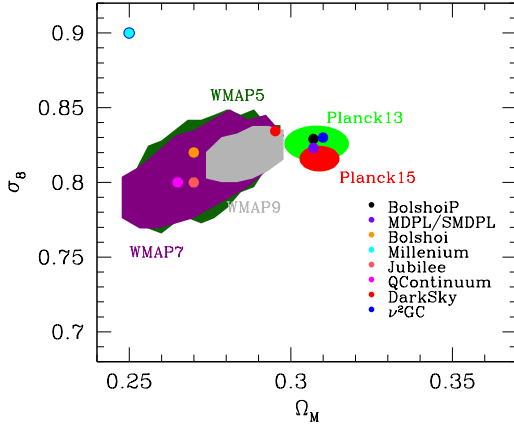


Figure 1. Observational constraints on σ_8 and Ω_M compared to values assumed in cosmological N -body simulations. The observations plotted are as follows: WMAP5+BAO+SN (Hinshaw et al. 2009), WMAP7+BAO+ H_0 (Jarosik et al. 2011), WMAP9+eCMB+BAO+ H_0 (Hinshaw et al. 2013a), Planck13+WP+highL+BAO (Planck Collaboration et al. 2014), and Planck15+TT,TE,EE+lowP+lensing+ext (Planck Collaboration et al. 2015a).

MultiDark (Prada et al. 2012; Riebe et al. 2013), Jubilee (Watson et al. 2013), DarkSky (Skillman et al. 2014), Q Continuum (Heitmann et al. 2015), ν^2 GC (Ishiyama et al. 2015), and Bolshoi-Planck and MultiDark-Planck (Klypin et al. 2014) simulations. Figure 1 shows the WMAP5/7/9 (Hinshaw et al. 2013b) and Planck 2013 (Planck Collaboration et al. 2014) and Planck 2015 (Planck Collaboration et al. 2015a) cosmological parameters σ_8 and Ω_M , and the cosmological parameters adopted for these simulations. The Millennium simulations used the first-year (WMAP1) parameters (Spergel et al. 2003); the Bolshoi, Q Continuum, and Jubilee simulations used the WMAP5/7 cosmological parameters; while the ν^2 GC and Bolshoi-Planck simulations used the Planck 2013 parameters, and the DarkSky simulations used parameters between WMAP9 and Planck 2013.

In this paper we use the ROCKSTAR halo finder (Behroozi, Wechsler & Wu 2013) and CONSISTENT TREES (Behroozi et al. 2013) to analyze results for the recent Bolshoi-Planck (BolshoiP), Small MultiDark-Planck (SMDPL) and MultiDark-Planck (MDPL) simulations based on the 2013 Planck cosmological parameters (Planck Collaboration et al. 2014) and compatible with the Planck 2015 parameters (Planck Collaboration et al. 2015a). The BolshoiP, SMDPL and MDPL simulations are not the largest of the new high-resolution simulations, but they do have the advantage that they have been analyzed in great detail, and all of these analyses are being made publicly available. In addition, in this paper we show the effects of the change from the WMAP5/7 to the Planck 2013 cosmological parameters.

In this paper we focus on the scaling relations of several basic halo properties, updating their scaling relations as a function of redshift for the Planck cosmological parameters as well as the redshift evolution of halo/subhalo number densities. For the majority of these halo properties we report fitting functions that can be very useful not only to gain in-

sight about the halo/subhalo population but also for the galaxy-halo connection and thus for galaxy evolution. Indeed, techniques such as subhalo abundance matching and halo occupation distribution models require as inputs the halo/subhalo number densities. Furthermore, simplified prescriptions for the evolution of dark matter halo properties are ideal tools for people interested in understanding average properties of halos and the galaxies that they host.

Here we analyze *all* dark matter halos and subhalos found by ROCKSTAR, and do not just focus on those that satisfy some criteria for being “relaxed” or otherwise “good,” in contrast to some earlier studies of dark matter halo properties (e.g., Bett et al. 2007; Macciò et al. 2007; Ludlow et al. 2014). The reason is that all sufficiently massive halos are expected to host galaxies or, for the more massive ones, groups or clusters of galaxies.

This paper is an introduction to a series of papers presenting additional analyses of the Bolshoi-Planck and MultiDark-Planck simulations. The statistics and physical meaning of halo concentration are discussed in detail in Klypin et al. (2014), which is also an overview of the Bolshoi-Planck and MultiDark-Planck simulations, including BigMultiDark simulations in $(2.5h^{-1}\text{Gpc})^3$ volumes that we do not discuss here since they are mainly useful for statistics of galaxy clusters. The Stellar Halo Accretion Rate Co-evolution (SHARC) assumption—i.e., that the star formation rate of central galaxies on the main sequence of star formation is proportional to their host halo’s mass accretion rate—was explored in Rodríguez-Puebla et al. (2016), which used abundance matching based on the Bolshoi-Planck simulation. That paper showed that SHARC is remarkably consistent with the observed galaxy star formation rate out to $z \sim 4$ and that the ~ 0.3 dex dispersion in the halo mass accretion rate is consistent with the observed small dispersion of the star formation rate about the main sequence. The clustering properties of halos and subhalos is the subject of Rodríguez-Puebla et al. 2016b (in prep.). How properties of dark matter halos vary with the density of their environment on length scales from 0.5 to 16 h^{-1} Mpc is discussed in Lee et al. (2016a, in prep.), which shows among other things that halos in low-density regions experience lower tidal forces and have lower spin parameters, and that a large fraction of lower-mass halos in high-density regions are “stripped,” i.e. their mass at $z = 0$ is less than that of their progenitors at higher redshifts. Another paper (Lee et al., 2016b, in prep.) studies the causes of halo stripping and properties of such stripped halos. Further papers comparing with observations are also in preparation, along with mock galaxy catalogs based on Bolshoi-Planck.

This paper is organized as follows: §2 discusses the simulations and how we define the halo mass. §3 describes the key scaling relations for distinct halos (i.e., those that are not subhalos) and gives figures and fitting formulas for maximum halo circular velocity (§3.1), halo mass accretion rates (§3.2) and mass growth (§3.3). §4 discusses halo (§4.1) and subhalo (§4.2) number densities, and the number of subhalos as a function of their host halo mass (§4.3). §5 presents the halo and subhalo velocity functions. §4 and §5 also compare the Planck cosmology halo mass and velocity functions with those from the WMAP5/7 cosmological parameters. §6 discusses the dependence of halo concentration and spin on mass and redshift. §7 discusses the evolution of the Tully-

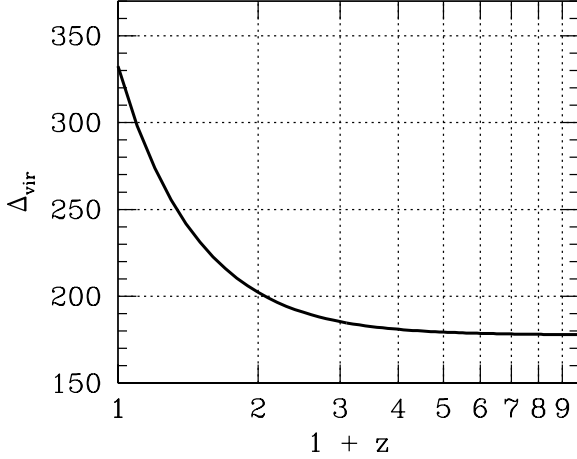


Figure 2. Virial overdensity Δ_{vir} given by the spherical collapse model (Bryan & Norman 1998). The value of the virial overdensity at $z = 0$ is $\Delta_{\text{vir}} = 333$ for the Bolshoi-Planck cosmological parameters, while for large z it approaches to $\Delta_{\text{vir}} = 178$.

Fisher and Faber-Jackson relations between halo circular velocity V_{max} and the stellar mass of the central galaxies in these halos. §8 compares the halo velocity function with the galaxy velocity function from optical and radio observations. §9 summarizes and briefly discusses the key results in this paper. Appendix A is an overview of the CONSISTENT TREES merger tree information and halo catalogs and Appendix B summarizes the ROCKSTAR and CONSISTENT TREES fields.

2 THE SIMULATIONS

The cosmological parameter values for the Bolshoi-Planck and MultiDark-Planck simulations are $\Omega_{\Lambda,0} = 0.693$, $\Omega_{M,0} = 0.307$, $\Omega_{B,0} = 0.048$, $h = 0.678$, $n_s = 0.96$ and $\sigma_8 = 0.823$. The parameters are the same for the MultiDark-Planck simulations except for $\sigma_8 = 0.829$. Simulation volumes, resolutions and other parameters of the Bolshoi and MultiDark simulations with WMAP7/9 parameters, and the new Bolshoi-Planck and the $(400h^{-1}\text{Mpc})^3$ and $(1h^{-1}\text{Gpc})^3$ MultiDark-Planck simulations are summarized in Table 1. The details about the number and redshift distribution of the saved timesteps of these simulations are given in Appendix A. Outputs from these simulations are available online at the CosmoSim website.¹ Entire ROCKSTAR and CONSISTENT TREES outputs are downloadable from another website.²

In this paper we define halo masses by using spherical overdensities according to the redshift-dependent virial overdensity $\Delta_{\text{vir}}(z)$ given by the spherical collapse model, for which Bryan & Norman (1998) give the fitting formula $\Delta_{\text{vir}}(z) = (18\pi^2 + 82x - 39x^2)/\Omega(z)$, where $\Omega(z)$ is the ratio of mean matter density ρ_m to critical density ρ_c at redshift

z , and $x \equiv \Omega(z) - 1$. Figure 2 shows the redshift dependence of Δ_{vir} for the cosmology of the Bolshoi-Planck simulation. The value of the virial overdensity at $z = 0$ is $\Delta_{\text{vir}} = 333$, while for large z it asymptotes to $18\pi^2 = 178$. The virial radius R_{vir} of a halo of virial mass M_{vir} is defined as the radius within which the mean density is Δ_{vir} times the mean matter density $\rho_m = \Omega_M \rho_c$ at that redshift. Then the virial halo mass is

$$M_{\text{vir}} = \frac{4\pi}{3} \Delta_{\text{vir}} \rho_m R_{\text{vir}}^3. \quad (1)$$

Another common choice employed to define halos is the radius R_{200c} enclosing 200 times critical density, with corresponding halo mass

$$M_{200c} = \frac{4\pi}{3} 200 \rho_c R_{200c}^3, \quad (2)$$

which was used in Klypin et al. (2014). Yet another common choice is R_{200m} enclosing 200 times mean density, with corresponding halo mass M_{200m} . Although we use M_{vir} in this paper, the ROCKSTAR/CONSISTENT TREES analyses of the Bolshoi-Planck and MultiDark-Planck simulations described in the Appendices include outputs for both M_{vir} and M_{200m} .

We note that Diemer, More & Kravtsov (2013) argued that much of the mass evolution of dark matter halos is an artifact caused by the changing radius of the halo as the mean cosmic matter density ρ_m declines as the universe expands. They call this phenomenon “pseudoevolution,” since the dark matter distribution in the interior of most halos hardly changes at low redshift (Prada et al. 2006; Diemand, Kuhlen & Madau 2007; Cuesta et al. 2008). Recently More, Diemer & Kravtsov (2015) proposed that the best physically-based definition of halo radius is the “splash-back radius” $R_{\text{sp}} \approx 2R_{200m}$, where there is typically a sharp drop in the density. Using this definition, there is actually more halo mass increase than for R_{vir} or R_{200m} . This is discussed further in Rodríguez-Puebla et al. (2016), where we argue that for purposes like predicting galaxy star formation, the R_{vir} definition used here works fine.

3 BASIC SCALING RELATIONS FOR DISTINCT HALOS

Galaxies form and evolve in dark matter halos, and it is expected that visible galaxies are hosted by all halos in the mass range $M_{\text{vir}} \gtrsim 10^{10.2} h^{-1} M_{\odot}$ where halos can be resolved with at least $\gtrsim 100$ particles in the BolshoiP and SMDPL simulations. Therefore, the statistical properties of dark matter halos, which can be studied in great detail in high resolution numerical N -body simulations, can provide hints on the nature of galaxy properties and spatial distributions. In this Section, we report dark matter halo velocity and mass and their scaling relations. Dependence on mass and redshift of halo concentration and spin are discussed in §6.

3.1 Maximum halo circular velocity

As usual, the circular velocity is defined as $V_{\text{circ}} \equiv \sqrt{GM(<r)}/r$, where $M(<r)$ is the halo mass enclosed by a sphere of radius r . Dark matter halos have circular velocity that grows from 0 at $r = 0$ to a maximum value V_{max} at

¹ <https://www.cosmosim.org/cms/simulations/multidark-project/> with explanations in Riebe et al. (2013) and at <https://www.cosmosim.org/cms/documentation/introduction/whats-different/> for users of the earlier site <http://www.multidark.org/>.

² <http://hipacc.ucsc.edu/Bolshoi/MergerTrees.html>

Table 1. Numerical and cosmological parameters for the simulations analyzed in this paper. The columns give the simulation identifier on the CosmoSim website, the size of the simulated box in h^{-1} Gpc, the number of particles, the mass per simulation particle m_p in units $h^{-1} M_\odot$, the Plummer equivalent gravitational softening length ϵ in units of physical h^{-1} kpc, the adopted values for Ω_{Matter} , Ω_{Baryon} , Ω_Λ , σ_8 , the spectral index n_s , and the Hubble constant H_0 in km/s/Mpc. The references for these simulations are (a) Klypin et al. (2014), (b) Klypin, Trujillo-Gomez & Primack (2011), (c) Prada et al. (2012).

Simulation	box	particles	m_p	ϵ	Ω_M	Ω_B	Ω_Λ	σ_8	n_s	H_0	Code	Ref.
BolshoiP	0.25	2048 ³	1.5×10^8	1.0	0.307	0.048	0.693	0.823	0.96	67.8	ART	a
SMDPL	0.4	3840 ³	9.6×10^7	1.5	0.307	0.048	0.693	0.829	0.96	67.8	GADGET-2	a
MDPL	1.0	3840 ³	1.5×10^9	5	0.307	0.048	0.693	0.829	0.96	67.8	GADGET-2	a
Bolshoi	0.25	2048 ³	1.3×10^8	1.0	0.270	0.047	0.730	0.820	0.95	70.0	ART	b
MultiDark	1.0	2048 ³	8.7×10^9	7.0	0.270	0.047	0.730	0.820	0.95	70.0	ART	c

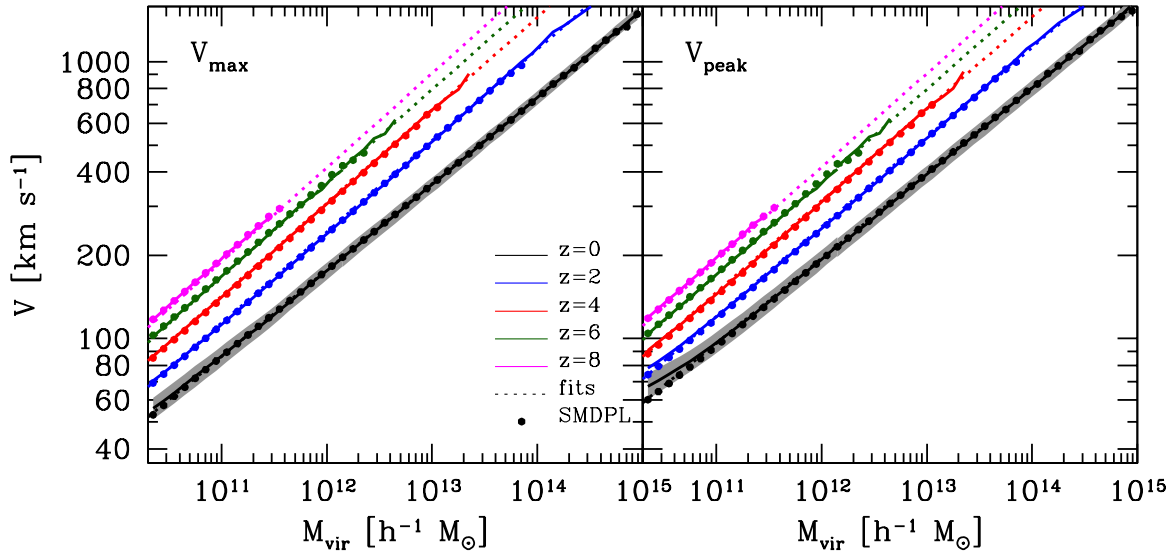


Figure 3. **Left Panel:** Maximum halo circular velocity, V_{max} , as a function of M_{vir} at $z = 0, 2, 4, 6$ and 8 . Medians are shown as the solid lines for the BolshoiP and MDPL simulations, filled circles are the medians of the SMDPL simulation. At $z = 0$ the grey band is the 68% range of the maximum circular velocity. The dotted lines show the fits to the simulation. A single power law is able to reproduce the results from the simulation. The slopes are approximately independent of redshift with a value of $\sim 1/3$. **Right Panel:** The highest maximum circular velocity reached along the main progenitor branch, V_{peak} , as a function of M_{vir} at $z = 0, 2, 4, 6$ and 8 . Similarly to the V_{max} panel, medians are shown as the solid lines. At $z = 0$ the grey band is the 1σ (68%) range of the maximum circular velocity. The dotted lines show the fits to the simulation. Also, the slopes are approximately independent of redshift with a value of $\sim 1/3$.

a radius R_{max} that is usually considerably less than R_{vir} . (§6.1 shows that for the NFW radial halo mass distribution, $R_{\text{max}} = 2.1626 \times R_s$.) Because V_{max} characterizes the inner halo, it may correlate better with the properties of the central galaxy than M_{vir} does. The left panel of Figure 3 shows the medians of the maximum halo circular velocity, V_{max} , as a function of M_{vir} at $z = 0, 2, 4, 6$ and 8 , solid lines. The grey band at $z = 0$ shows the 68% range of the maximum circular velocity, i.e., the halo distribution between the 16th and 84th percentiles. We find that the 68% range of the distribution is approximately independent of redshift and halo mass, with a value of ~ 0.05 dex. In general, the $V_{\text{max}}-M_{\text{vir}}$ relation follows a power law-fit at all redshifts and over the mass range where we can resolve distinct halos in the Bolshoi-Planck simulations, $M_{\text{vir}} \sim 10^{10.2} M_\odot$. To a good approximation, the $V_{\text{max}}-M_{\text{vir}}$ slope is given by $\alpha \sim 1/3$,

as expected from spherical collapse. In reality, however, the slope depends slightly on redshift as we will quantify below.

Distinct halos can lose mass due to stripping events as a result of interactions with other halos. In consequence, the maximum halo circular velocity V_{max} can significantly decrease. This reduction in V_{max} can introduce an extra source of uncertainty when relating galaxies to dark matter halos, since it is expected that stripping would affect halos more significantly than the central galaxies deep inside them. Therefore, in the case of stripped halos, the correlation between the present V_{max} of the halo and galaxy stellar mass/luminosity is not trivial. Indeed, Moster et al. (2010) and Reddick et al. (2013) found that the highest maximum circular velocity reached along the halo's main progenitor branch, V_{peak} , is a better halo proxy for galaxy stellar mass/luminosity. For these reasons we find it useful to report the $V_{\text{peak}}-M_{\text{vir}}$ relation in this paper.

The right panel of Figure 3 shows the redshift evolution of the highest maximum circular velocity reached along the main progenitor branch, V_{peak} , as a function of M_{vir} at $z = 0, 2, 4, 6$ and 8 . As for $V_{\text{max}}-M_{\text{vir}}$, medians are shown as the solid lines. The grey band at $z = 0$ is the 68% of the distribution. We find that the slope depends more on redshift than for the $V_{\text{max}}-M_{\text{vir}}$ relation. The differences in the slopes, especially at lower redshifts, are a consequence of tidal stripping events, as mentioned above. On the other hand, we find that the scatter is independent of redshift and mass and of the order of ~ 0.05 dex, similarly to $V_{\text{max}}-M_{\text{vir}}$.

The dotted lines in Figure 3 show power-law fits to the BolshoiP, SMDPL and MDPL simulations both for the $V_{\text{max}}-M_{\text{vir}}$ (left panel) and $V_{\text{peak}}-M_{\text{vir}}$ (right panel) relationships. We motivate the power law-fits based on the well known results for isothermal dark matter halo profiles. For a singular isothermal sphere the circular velocity (assumed to be independent of radius inside the halo) evolves with redshift as

$$V_{\text{max}} \propto [M_{\text{vir}} E(z)]^{1/3}, \quad (3)$$

where $E(z)$ is the expansion rate H/H_0 for a flat universe:

$$E(z) = \sqrt{\Omega_{\Lambda,0} + \Omega_{\text{m},0}(1+z)^3}. \quad (4)$$

Of course this is a simplification since the mass profile of dark matter halos is markedly different from an isothermal sphere as previous studies based on high-resolution N -body simulations have shown (for a recent discussion see: Klypin et al. 2015). However, the general structure of Equation (3) can be useful to suggest fitting functions for redshift evolution. Based on this, we assume the following parametric form for the redshift evolution both for the $V_{\text{max}}-M_{\text{vir}}$ and $V_{\text{peak}}-M_{\text{vir}}$ relationships

$$V(M_{\text{vir}}, z) = \beta(z) [M_{\text{vir},12} E(z)]^{\alpha(z)}, \quad (5)$$

where $M_{\text{vir},12} \equiv M_{\text{vir}}/(10^{12} h^{-1} \text{M}_{\odot})$. Our fitting functions for $V_{\text{max}}-M_{\text{vir}}$, with a representing the scale factor $a = 1/(1+z)$, are

$$\alpha(z) = 0.346 - 0.059a + 0.025a^2, \quad (6)$$

and

$$\log \beta(z) = 2.209 + 0.060a - 0.021a^2, \quad (7)$$

while the fitting functions for $V_{\text{peak}}-M_{\text{vir}}$ are

$$\alpha(z) = 0.346 - 0.080a + 0.042a^2, \quad (8)$$

and

$$\log \beta(z) = 2.205 + 0.150a - 0.063a^2. \quad (9)$$

3.2 Halo mass accretion rates

Halo mass accretion is responsible for controlling the rate at which the baryonic mass, M_b , is deposited in galaxies. In the past, instantaneous halo mass accretion rates, dM_{vir}/dt , have been studied in great detail based on the Extended Press-Schechter formalism (Kauffmann & White 1993; Lacey & Cole 1993; Somerville & Kolatt 1999; van den Bosch 2002; Neistein, van den Bosch & Dekel 2006; Zhang, Fakhouri & Ma 2008; Firmani & Avila-Reese 2013) or high-resolution N -body simulations (Wechsler et al. 2002; Cohn & White 2005; McBride, Fakhouri & Ma

2009; Tweed et al. 2009; Fakhouri, Ma & Boylan-Kolchin 2010; Srisawat et al. 2013) or either both (Parkinson, Cole & Helly 2008; Jiang & van den Bosch 2014; van den Bosch et al. 2014). In addition to instantaneous halo mass accretion rates dM_{vir}/dt calculated between stored simulation timesteps, in this paper we extend the above work by also studying halo mass accretion rates averaged over the dynamical time $dM_{\text{vir,dyn}}/dt$, defined as

$$\left\langle \frac{dM_{\text{vir}}}{dt} \right\rangle_{\text{dyn}} = \frac{M_{\text{vir}}(t) - M_{\text{vir}}(t - t_{\text{dyn}})}{t_{\text{dyn}}}, \quad (10)$$

where the dynamical time of the halo is $t_{\text{dyn}}(z) = [G\Delta_{\text{vir}}(z)\rho_{\text{m}}(z)]^{-1/2}$. The ratio of the dynamical time to the Hubble time $t_H = H^{-1}$ is $t_{\text{dyn}}/t_H = [(8\pi)/(3\Delta_{\text{vir}}\Omega_{\text{M}})]^{1/2}$, which equals 0.29 at $a = 0$ and asymptotes to 0.22 at high redshift. We also report halo mass accretion rates of the maximum mass M_{peak} reached along the main progenitor branch averaged from the current halo's redshift, z , to $z + 0.5$, dM_{peak}/dt . For more details the reader is referred to Appendix B4.

Figure 4 shows the medians of halo mass accretion rates at $z = 0, 2, 4, 6$ and 8 . The upper panel shows the instantaneous halo mass accretion rate, dM_{vir}/dt , while the left and right bottom panels show halo mass accretion rates averaged over a dynamical time, $dM_{\text{vir,dyn}}/dt$, and M_{peak} halo accretion rates, dM_{peak}/dt , respectively. The grey band at $z = 0$ in all the panels shows the distribution of halo mass accretion rates between the 16th and 84th percentiles, i.e., the 68% of the distribution. We find that the dispersion is roughly independent of redshift and in slightly dependent on halo mass. The dispersion for dM_{vir}/dt is roughly ~ 0.35 dex, while for $dM_{\text{vir,dyn}}/dt$ is ~ 0.25 dex, and for dM_{peak}/dt is ~ 0.3 dex. The $dM_{\text{vir}}/dt - M_{\text{vir}}$ relations follow a power law-fit, especially at high redshifts. As a crude estimation, the slope for the $dM_{\text{vir}}/dt - M_{\text{vir}}$ relations is $\alpha \sim 1.1$, consistent with previous studies based on the Press-Schechter formalism (e.g., Neistein, van den Bosch & Dekel 2006) and the Millennium and Millennium-II high resolution N -body simulations (Fakhouri, Ma & Boylan-Kolchin 2010).

The dotted lines in Figure 5 show power-law fits to the simulations for the halo mass accretion rates, given by

$$\frac{dM_{\text{vir}}}{dt} = \beta(z) M_{\text{vir},12}^{\alpha(z)} E(z), \quad (11)$$

where

$$\log \beta(z) = \beta_0 + \beta_1 a + \beta_2 a^2, \quad (12)$$

and

$$\alpha(z) = \alpha_0 + \alpha_1 a + \alpha_2 a^2. \quad (13)$$

Table 2 lists the best fit parameters for the $dM_{\text{vir}}/dt - M_{\text{vir}}$ relations. Power-law fits can provide an accurate description for both $dM_{\text{vir,dyn}}/dt$ and dM_{peak}/dt for the three simulations.

As can be observed in the upper panel of Figure 4, however, a power-law fit is a poor description of the instantaneous halo mass accretion rates, especially for the BolshoiP and MDPL simulations at low masses and low redshifts. In order to find a better description of the instantaneous halo mass accretion rates for the BolshoiP and MDPL simulations we use a double power-law fit

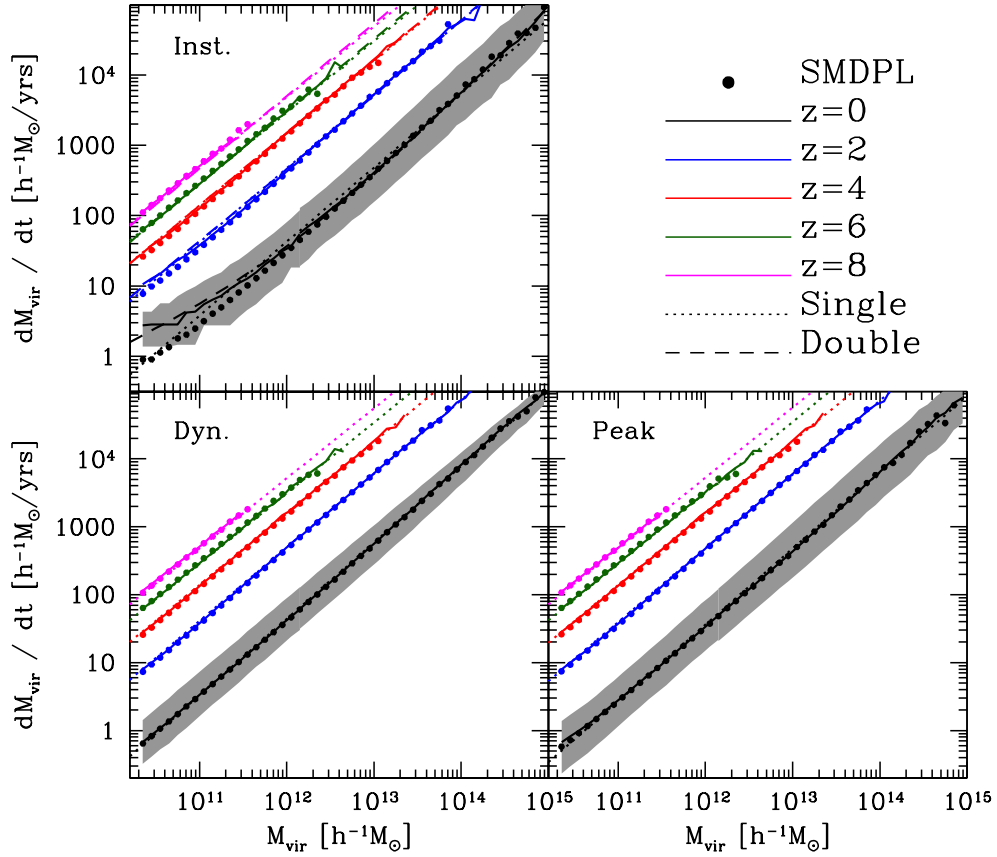


Figure 4. Halo mass accretion rates as a function of M_{vir} at $z = 0, 2, 4, 6$ and 8 . Medians are shown as the solid lines for the BolshoiP and MDPL simulations, and filled circles are the same for the SMDPL simulation. At $z = 0$ the grey band is the 68% range of halo mass accretion rates for the BolshoiP and MDPL simulations. The dotted lines show the fits to the simulations when using a power law, Equation (11). **Upper Panel:** Instantaneous halo mass accretion rates. The long dashed line shows the fits using a double power law, Equation (14), for the BolshoiP and MDPL simulations. **Bottom Left Panel:** Halo mass accretion rates averaged over a dynamical time. A single power law reproduces the results from the simulations. The slopes are approximately independent of redshift with a value of ~ 1.1 . **Bottom Right Panel:** Mass accretion rates of M_{peak} averaged from the current halo’s redshift, z , to $z + 0.5$. As for the dynamical time averaged accretion rates, a single power law again reproduces the results from the simulations. The slopes are approximately independent of redshift with a value of ~ 1.1 .

Table 2. Best fit parameters for the $dM_{\text{vir}}/dt - M_{\text{vir}}$ relationships.

$dM_{\text{vir}}/dt [h^{-1}M_{\odot}/\text{yr}]$	α_0	α_1	α_2	β_0	β_1	β_2
Instantaneous	0.975	0.300	-0.224	2.677	-1.708	0.661
Dynamical averaged	0.997	0.328	-0.200	2.711	-1.739	0.672
Peak	1.000	0.329	-0.206	2.730	-1.828	0.654

$$\frac{dM_{\text{vir}}}{dt} = \beta(z)[M_{\text{vir},12}^{\alpha(z)} + M_{\text{vir},12}^{\gamma(z)}]E(z), \quad (14)$$

where the normalization is given by

$$\log \beta(z) = 2.437 - 1.857 \times a + 0.685 \times a^2, \quad (15)$$

and the powers $\alpha(z)$ and $\gamma(z)$ are given respectively by

$$\alpha(z) = 1.120 - 0.609 \times a + 0.097 \times a^2, \quad (16)$$

and

$$\alpha(z) = 0.917 + 0.845 \times a - 0.532 \times a^2. \quad (17)$$

The dashed lines in Figure 4 show this fit to the simulations.

Finally, based on the above definitions of halo accretion rates, the rate at which the cosmological baryonic inflow material is accreted into the dark matter halo is calculated as $dM_{\text{c,b}}/dt = f_{\text{c,b}} \times dM_{\text{vir}}/dt$, where the cosmic baryon fraction is $f_{\text{c,b}} \equiv \Omega_{\text{B},0}/\Omega_{\text{M},0} = 0.156$ for our cosmology. The rate $dM_{\text{c,b}}/dt$ is an important quantity; it equals the star formation rate plus the gas outflow rate if the galaxy is in “equilibrium” in bathtub model terms (e.g., Mitra, Davé & Finlator 2015, and references therein).

Galaxies can be divided into two main groups: star-forming and quiescent. Star-forming galaxies are typically

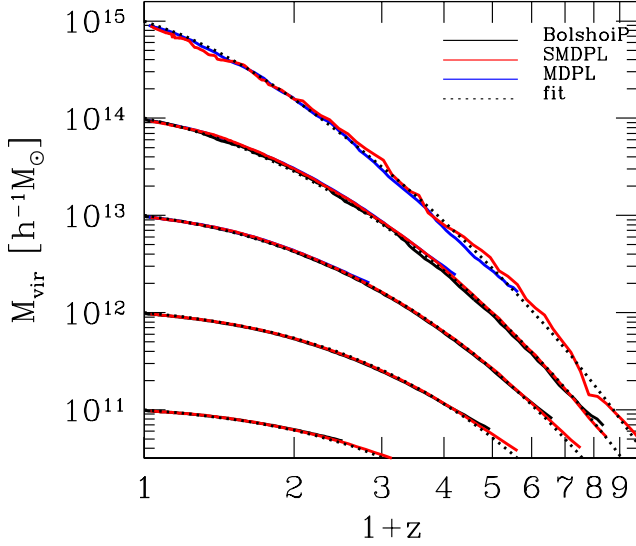


Figure 5. Median halo mass growth for progenitors $z = 0$ with masses of $M_{\text{vir}} = 10^{11}, 10^{12}, 10^{13}$, and $10^{14} h^{-1} M_{\odot}$, solid lines. Fits to simulations are shown with the dotted lines. The shaded area shows the dispersion around the medians.

blue young disk galaxies, while many quiescent galaxies are red old spheroids. These properties are partially determined by the mass of the dark matter halo in which they reside but, due to the complexity of the galaxy formation process, a dependence on other halo and/or environmental properties is expected. For example, star-forming galaxies at a given redshift are known to show a tight dependence of star formation rates on stellar mass, which is known as the “main sequence” of galaxy formation. The slopes and dispersions of halo mass accretion rates reported above are very similar to the observed dispersion and slope of the star formation rates on the main sequence. This naturally suggests that the halo mass accretion rate is controlling not only the baryon fraction that is entering the galaxies, but also their star formation efficiency. The galaxy stellar-to-halo mass relation is known to be nearly independent of redshift from $z = 0$ out to $z \sim 4$ (Behroozi, Wechsler & Conroy 2013a), so the galaxy star formation rate is determined on average by the mass accretion rate of the halo in which it resides: $dM_*/dt = (dM_*/dM_{\text{vir}})(dM_{\text{vir}}/dt)$. A recent paper by some of us, Rodríguez-Puebla et al. (2016), made the stronger assumption that this is true halo by halo for star-forming galaxies, which we called Stellar-Halo Accretion Rate Coevolution (SHARC). We showed that the SHARC assumption predicts galaxy star formation rates on the main sequence that are in good agreement with observations up to $z \sim 4$, and that in addition it approximately matches the small observed dispersion of ~ 0.3 dex of the galaxy star formation rates about the main sequence.

3.3 Halo assembly

Figure 5 presents the medians of the halo mass growth for progenitors at $z = 0$ with masses of $M_{\text{vir}} = 10^{11}, 10^{12}, 10^{13}, 10^{14}$ and $10^{15} h^{-1} M_{\odot}$, for the BolshoiP (black solid line) SMDPL (red solid line) and MDPL (blue solid line) simulations. In order to avoid resolution effects

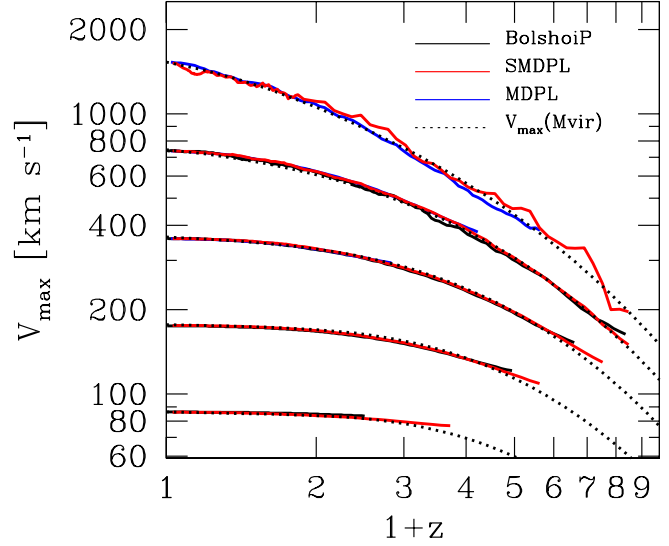


Figure 6. Median V_{max} growth for progenitors with masses of $M_{\text{vir}} = 10^{11}, 10^{12}, 10^{13}$, and $10^{14} h^{-1} M_{\odot}$, solid lines. Fits to simulations are shown with the dotted lines. The shaded area shows the dispersion around the medians.

and thus obtain reliable statistics we require that at every redshift at least 90% of the halos can be resolved with at least 100 particles. The first thing to note is that the three simulations agree with each other at all redshifts. From the figure it is evident that high mass halos assembled more rapidly at later epochs than lower mass halos. This is consistent with the fact the slopes obtained for halo mass accretion rates are slightly greater than 1. For the Planck cosmology we find that $10^{12} h^{-1} M_{\odot}$ halos formed half of their mass by $z \sim 1.2$. Progenitors of $M_{\text{vir}} = 10^{13}, 10^{14}$, and $10^{15} h^{-1} M_{\odot}$ halos reached the mass of $10^{12} h^{-1} M_{\odot}$ at $z \sim 2.5, 3.9$, and $z \sim 5$ respectively. Theoretically, the characteristic mass of $10^{12} h^{-1} M_{\odot}$ is expected to mark a transition above which the formation of stars in galaxies becomes increasingly inefficient. The reasons for this are that at halo masses above $10^{12} h^{-1} M_{\odot}$ the efficiency at which the virial shocks can heat the gas increases (e.g., Dekel & Birnboim 2006), and the gas can be kept from cooling by energy emitted from accretion onto supermassive black holes in these high-mass halos. Thus central galaxies in massive halos are expected to become passive systems roughly at the epoch when the halo reached the mass of $10^{12} h^{-1} M_{\odot}$. Note that Figure 2 of Ludlow et al. (2016) is similar to Figure 5, including also a comparison to warm dark matter cosmologies.

In order to characterize the growth of dark matter halos we use the fitting function from Behroozi, Wechsler & Conroy (2013b)

$$M_{\text{vir}}(M_{\text{vir}}(0), z) = M_{13}(z) 10^{f(M_{\text{vir}}(0), z)} \quad (18)$$

where

$$M_{13}(z) = 10^{13.6} h^{-1} M_{\odot} (1+z)^{2.755} (1+\frac{z}{2})^{-6.351} \exp(-0.413z) \quad (19)$$

$$f(M_{\text{vir}}, z) = \log \left(\frac{M_{\text{vir}}(0)}{M_{13}(0)} \right) \frac{g(M_{\text{vir}}(0), 1)}{g(M_{\text{vir}}(0), a)} \quad (20)$$

$$g(M_{\text{vir}}(0), a) = 1 + \exp[-3.676(a - a_0(M_{\text{vir}}(0)))] \quad (21)$$

Table 3. Best fit parameters to the Tinker et al. (2008) halo mass function Equations (25) and (32).

χ_i	$\chi_{0,i}$	$\chi_{1,i}$	$\chi_{2,i}$
A	0.144	-0.011	0.003
a	1.351	0.068	0.006
b	3.113	-0.077	-0.013
c	1.187	0.009	0.000

$$a_0(M_{\text{vir}}(0)) = 0.592 - \log \left[0.113 \left(\frac{10^{15.7} h^{-1} M_{\odot}}{M_{\text{vir}}(0)} \right) + 1 \right]. \quad (22)$$

As is emphasized in Behroozi, Wechsler & Conroy (2013b), as opposed to other previous descriptions, the above parameterization avoids the problem that progenitor histories of halos with different masses cross.

Figure 6 presents the medians of the maximum circular velocity growth for the progenitors of halos of the same masses $M_{\text{vir}} = 10^{11}$ to $10^{15} h^{-1} M_{\odot}$ described above. The maximum circular velocity is more directly connected to the central potential depth of the halo than the virial circular velocity or mass (see e.g., van den Bosch et al. 2014), and presumably more connected to the formation of the host galaxy. We find that for halos of $M_{\text{vir}} = 10^{11} h^{-1} M_{\odot}$, V_{max} is practically constant after $z \sim 2$, while for halos of $M_{\text{vir}} = 10^{12} h^{-1} M_{\odot}$ and $M_{\text{vir}} = 10^{13} h^{-1} M_{\odot}$, V_{max} is constant since $z \sim 1$ and $z \sim 0.5$, respectively. This is consistent with the fact that the interiors of halos hardly change at low redshifts (Prada et al. 2006; Diemand, Kuhlen & Madau 2007; Cuesta et al. 2008). The dotted line in Figure 6 shows the growth of V_{max} when combining Equations (5) and (18). This simple prescription reproduces accurately the redshift dependence of halo V_{max} growth.

4 HALO AND SUBHALO NUMBER DENSITIES

4.1 Distinct halo mass function

The comoving number density of distinct halos at the mass range $\log M_{\text{vir}}$ and $\log M_{\text{vir}} + d \log M_{\text{vir}}$, i.e., the halo mass function ($dn_{\text{h}}/d \log M_{\text{vir}}$), are presented in the left panel of Figure 7 both for the Bolshoi-Planck and MD-Planck simulations. The right panel of the same figure shows the cumulative comoving number density, $n_{\text{h}}(> M_{\text{vir}})$. We compare the measured halo mass function from the simulations to the analytical fitting formula reported in Tinker et al. (2008), which we find provides accurate fits to the results of the Bolshoi-Planck and MD-Planck simulations at low redshifts. At high redshifts, however, it tends to underestimate $dn_{\text{h}}/d \log M_{\text{vir}}$ (see also Klypin et al. 2014).

Theoretically, the comoving number density of halos at the mass range M_{vir} and $M_{\text{vir}} + dM_{\text{vir}}$ is given by

$$\frac{dn_{\text{h}}}{dM_{\text{vir}}} = f(\sigma) \frac{\rho_m}{M_{\text{vir}}^2} \left| \frac{d \ln \sigma^{-1}}{d \ln M_{\text{vir}}} \right|. \quad (23)$$

where σ is the amplitude of the perturbations and $f(\sigma)$ is the

halo multiplicity function. The cumulative number density of halos above the mass M_{vir} is simply:

$$n_{\text{h}}(> M_{\text{vir}}) = \int_{M_{\text{vir}}}^{\infty} \frac{dn_{\text{h}}}{d \log M_{\text{vir}}} d \log M_{\text{vir}}. \quad (24)$$

In this paper we use the parametrization given in Tinker et al. (2008):

$$f(\sigma) = A \left[\left(\frac{\sigma}{b} \right)^{-a} + 1 \right] e^{-c/\sigma^2}. \quad (25)$$

The amplitude of the perturbations is given by

$$\sigma^2(M_{\text{vir}}, a) = \frac{D^2(a)}{2\pi^2} \int P(k) k^2 W^2(k, M_{\text{vir}}) dk, \quad (26)$$

where $P(k)$ is the power spectrum of perturbations and $W^2(k, M_{\text{vir}})$ is a window function defined to be the Fourier transform of the real-space top-hat filter of a sphere of mass M_{vir} and $D(a)$ is the linear growth-rate factor of the perturbations given by the expression

$$D(a) = \frac{g(a)}{g(1)}, \quad (27)$$

where to a good approximation $g(a)$ is given by (Lahav et al. 1991):

$$g(a) = \frac{\frac{5}{2} \Omega_m(a) a}{\Omega_m(a) - \Omega_{\Lambda}(a) + [1 + \frac{1}{2} \Omega_m(a)]/[1 + \frac{1}{70} \Omega_{\Lambda}(a)]}. \quad (28)$$

Figure 8 shows the amplitude of perturbations, $\sigma(M_{\text{vir}})$, as a function of M_{vir} for $a = 1$. The red solid line is calculated based on the transfer function from CAMB (Lewis, Challinor & Lasenby 2000). Following Klypin, Trujillo-Gomez & Primack (2011), we find that the amplitude of perturbations σ is well given by

$$\sigma(M_{\text{vir}}) = \frac{17.111 y^{0.405}}{1 + 1.306 y^{0.22} + 6.218 y^{0.317}}, \quad (29)$$

with $y = 1/M_{\text{vir},12}$. Note that the above fit is only valid for the Bolshoi-Planck cosmology studied in this paper. The dashed line in Figure 8 shows the best fitting model for $\sigma(M_{\text{vir}})$ given by the above equations.

The characteristic mass $M_C(z)$ of halos just collapsing at redshift z is given by $\nu = 1$ in

$$\nu = \frac{\delta_c}{\sigma(M_C, z)}. \quad (30)$$

where $\delta_c = 1.686$ for uniform-density spherical collapse. Figure 9 shows the Characteristic halo mass M_C as a function of redshift, red solid line. Note the strong dependence with redshift. For our cosmology, at $z = 0$ we find that $M_C \sim 5 \times 10^{12} h^{-1} M_{\odot}$ while at $z = 1, 2$ and 5 we find that $M_C \sim 1.5 \times 10^{11}, 6.3 \times 10^9$ and $7.6 \times 10^8 h^{-1} M_{\odot}$, respectively. We find that to good accuracy the redshift dependence of M_C is given by the following fitting function,

$$\log M_C(a) = 12.68 - 0.084 y^{0.01} - 5.33 y^{1.92} - 8.22 y^{7.8}, \quad (31)$$

where $y \equiv z/(1+z) = 1-a$.

Next, we update the best fitting parameters to the Tinker et al. (2008) formulae for the virial halo mass definition for the Planck cosmology. In order to find the best fitting parameters to the redshift evolution of the halo mass function we will assume the following redshift dependence for the parameters $\chi_i = A, a, b$ and c in Equation (25),

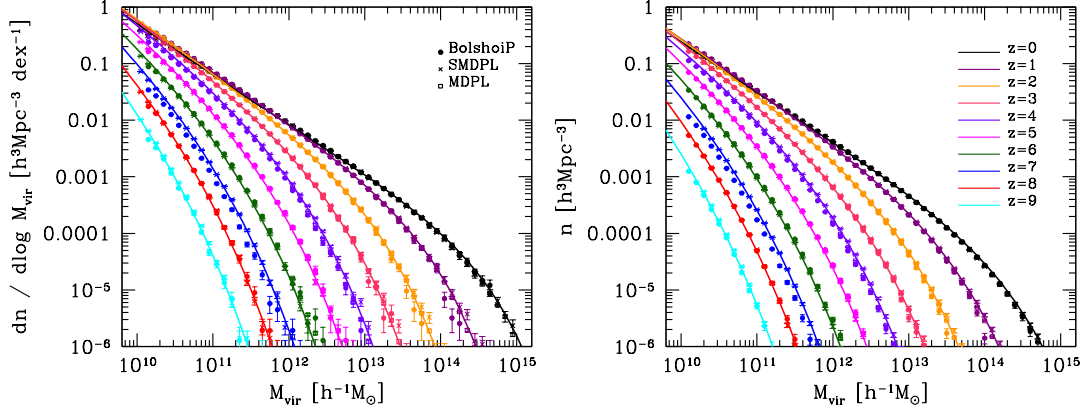


Figure 7. **Left Panel:** The halo mass function from $z = 0$ to $z = 9$. **Right Panel:** Cumulative halo mass function. The various solid lines show the fits to the simulations, Equation (25).

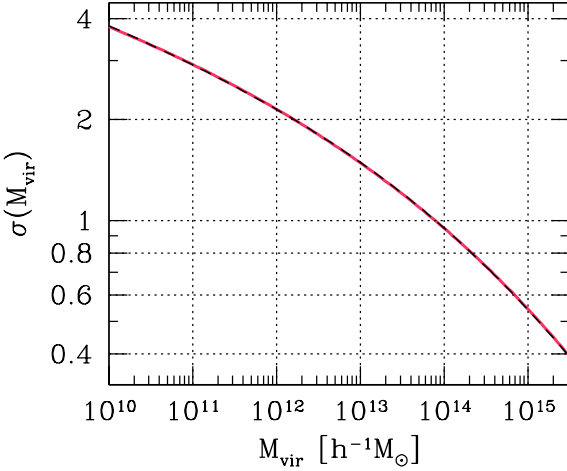


Figure 8. Amplitude of linear perturbations, $\sigma(M_{\text{vir}})$, as a function of M_{vir} . The red solid line shows the numerical solution to Equation (26). The dashed black line shows the fit to the amplitude of perturbations given by Equation (29).

$$\chi_i = \chi_{0,i} + \chi_{1,i}z + \chi_{2,i}z^2. \quad (32)$$

Table 3 lists the best fit parameters to the redshift evolution of the halo mass function. In the left panel of Figure 7 we present the best fits to the resulting halo mass functions from the simulations. For completeness, in the right panel of the same Figure we also show the resulting cumulative halo mass function using the best fit parameters from table 3.

Figure 10 shows the ratio of the number densities n_{BP} and n_{B} between the Bolshoi-Planck and the Bolshoi simulations as a function of M_{vir} from $z = 0$ to $z = 8$. The different cosmological parameters imply that at $z = 0$, on average, there are $\sim 12\%$ more Milky-Way mass halos in the Bolshoi-Planck than in the Bolshoi simulation. This fraction increases to higher masses, $\sim 25\%$ for $M_{\text{vir}} \sim 3 \times 10^{13} h^{-1} M_{\odot}$. This fraction also increases with redshift, and we find that at $z = 2, 4$ and 6 there are $\sim 25, 40$ and 60% more Milky-Way mass halos in the Bolshoi-Planck than in the Bolshoi

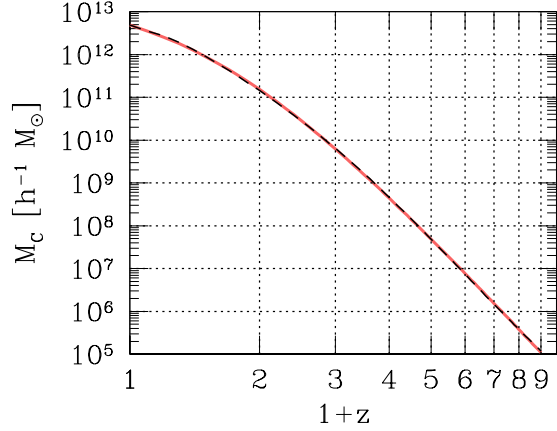


Figure 9. Characteristic halo mass M_C as a function of redshift. The red solid line shows the numerical solution to Equation (30). The dashed black line shows our numerical fit to M_C given by Equation (29).

simulation. At $z = 8$, there are about 3 times as many $M_{\text{vir}} = 10^{11} h^{-1} M_{\odot}$ halos in Bolshoi-Planck as in Bolshoi.

In the cold dark matter cosmology it is predicted that the number density of dark matter halos is a strong function of halo mass at low masses $dn_{\text{h}}/dM_{\text{vir}} \propto M_{\text{vir}}^{-1.8}$. In contrast, the observed galaxy stellar mass function, as well as the luminosity function, has a slope that is flatter. Recent analysis have found slopes between $\alpha \sim 1.4 - 1.6$ (Blanton et al. 2005; Baldry, Glazebrook & Driver 2008; Baldry et al. 2012) meaning that, for some reason, the star formation efficiency in low mass halos has been suppressed (e.g. Behroozi, Wechsler & Conroy 2013b; Moster, Naab & White 2013). Nevertheless, measurements of the baryonic mass have found slopes as steep as $\alpha \sim 1.9$ (Baldry, Glazebrook & Driver 2008).

4.2 Subhalo mass function

Subhalos can lose a significant fraction of their mass due to tidal stripping. Since tidal stripping affects the dark matter more than the stars of the central galaxy deep inside

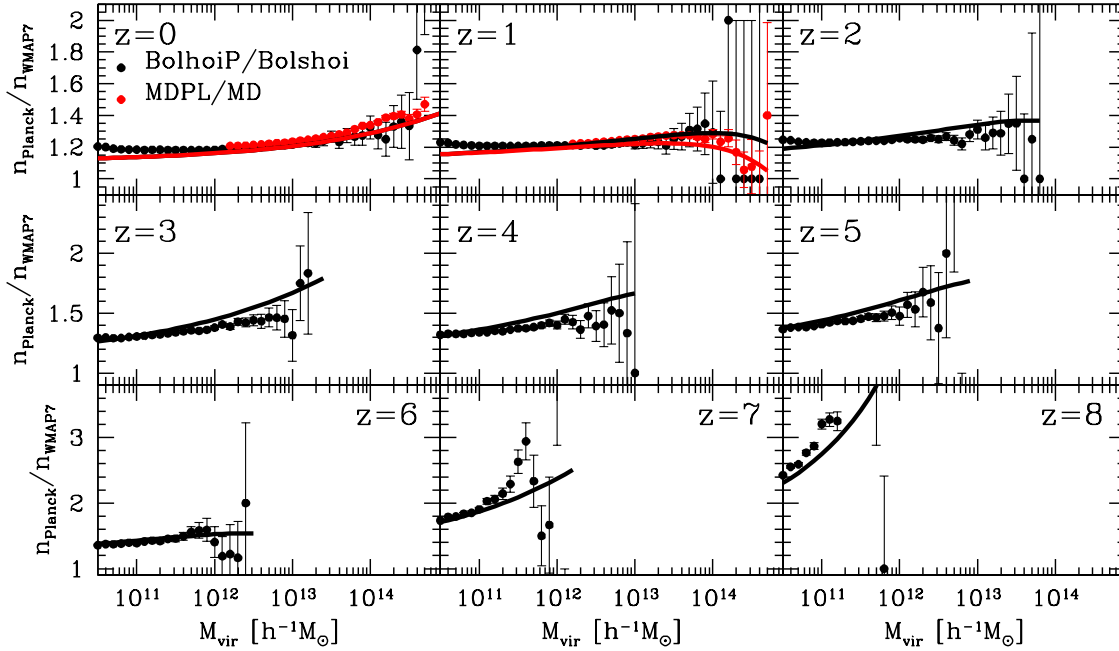


Figure 10. The ratio of the number densities of distinct halos between the Bolshoi-Planck n_{BP} and the Bolshoi n_{B} simulations as a function of M_{vir} from $z = 0$ to $z = 8$ are shown as filled circles, and the ratio of the fitting functions are shown as solid lines.

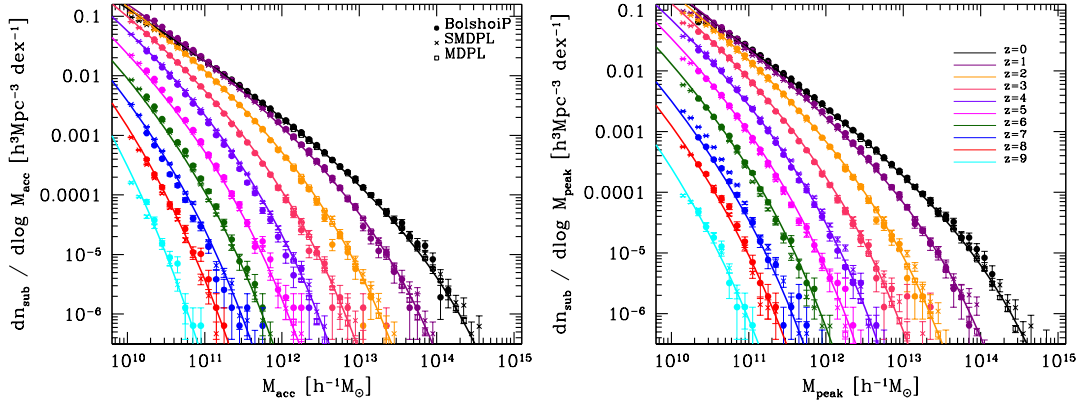


Figure 11. Subhalo mass M_{acc} (left panel) and M_{peak} (right panel) functions are shown for redshifts from $z = 0$ to 9 , along with fitting functions Equations (34) to (36).

the halo, this means that the correlation between galaxy stellar mass and present subhalo mass is not trivial. Therefore in approaches for connecting galaxies to dark matter (sub)halos, such as the abundance matching technique, it has been shown that the mass the subhalo had when it was still a distinct halo correlates better with the stellar mass of the galaxy it hosts. This comes from the fact that when assuming identical stellar-to-halo mass relations for central and satellite galaxies, the observed two-point correlation function is reproduced. Therefore it is useful to report the subhalo mass function when subhalos were accreted for the first time into a bigger distinct halo, i.e., the comoving number density of subhalos at the mass range $\log M_{\text{acc}}$ and

$\log M_{\text{acc}} + d \log M_{\text{acc}}$. In addition, we also present results for M_{peak} in the Bolshoi-Planck simulations. Similarly to V_{peak} , M_{peak} is defined as the maximum mass reached along the main progenitor assembly mass. Figure 11 shows the redshift evolution of the subhalo mass function, $dn_{\text{sub}}/d\log M_{\text{sub}}$, derived from the Bolshoi-Planck and MD-Planck simulations. The solid circles in the left panel show the resulting subhalo mass function for M_{acc} while the results for M_{peak} are shown in the right panel of the same figure.

The solid lines in Figure 11 show our best fitting models to the redshift evolution of the subhalo mass function. Previous reports of the mean number of subhalos above some mass M_{sub} at a given host of mass M_{vir} have

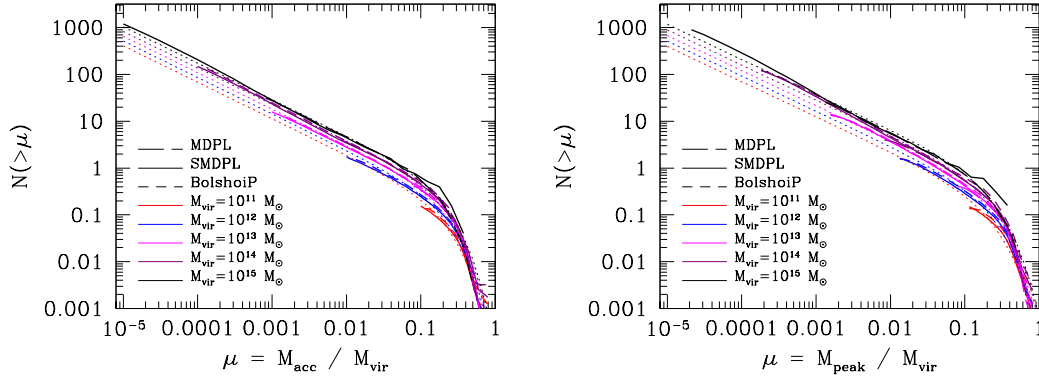


Figure 12. The cumulative subhalo mass function for different host halos as a function of $\mu = M_{\text{acc}}/M_{\text{vir}}$ and $M_{\text{peak}}/M_{\text{vir}}$ is shown as solid curves. The dotted curve is the fitting function Equation (37).

Table 4. Best fit parameters for the subhalo mass function.

Parameter	M_{acc}	M_{peak}
C_0	-0.1213	-0.0863
C_1	0.0113	0.0087
C_2	-0.0168	-0.0113
C_3	-0.0032	-0.0039
C_4	0.0005	0.0004
$\alpha_{\text{sub},1}$	0.1810	0.0724
$\alpha_{\text{sub},2}$	0.2138	0.2206
M_0	11.1416	11.9046
M_1	-0.6595	-0.6364
M_2	-0.0015	-0.02069
M_3	0.0183	0.0220
M_4	-0.00164	-0.0012

found that this is nearly independent of host mass and scales as $\langle N_{\text{sub}}(> M_{\text{sub}} | M_{\text{vir}}) \rangle \propto (M_{\text{sub}}/M_{\text{vir}})^\alpha$ with $\alpha \sim -1$, see also below. This implies that to a good approximation the subhalo mass function is $dn_{\text{sub}}/d\log M_{\text{sub}} \propto M_{\text{vir}}^\alpha dn_{\text{h}}/d\log M_{\text{vir}}$ (see e.g., Behroozi, Wechsler & Conroy 2013b). Here we generalized the fitting model proposed in Behroozi, Wechsler & Conroy (2013b) for the redshift evolution of the subhalo mass function for both M_{acc} and M_{peak} :

$$\frac{dn_{\text{sub}}}{d\log M_{\text{sub}}} = C_{\text{sub}}(z) G(M_{\text{vir}}, z) \frac{dn_{\text{h}}}{d\log M_{\text{vir}}}, \quad (33)$$

where

$$\log C_{\text{sub}}(z) = C_0 + C_1 a + C_2 a^2 + C_3 a^3 + C_4 a^4, \quad (34)$$

and

$$G(M_{\text{vir}}, z) = X^{\alpha_{\text{sub},1}} \exp(-X^{\alpha_{\text{sub},2}}), \quad (35)$$

where $X = M_{\text{vir}}/M_{\text{cut}}(z)$. The fitting function for $M_{\text{cut}}(z)$ is given by

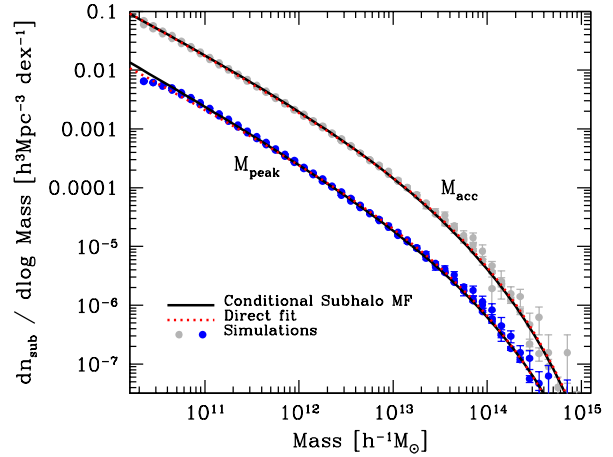


Figure 13. Comparison between the measured subhalo mass function from the BolshoiP, SMDPL and MDPL simulations and by computing $dn_{\text{sub}}/d\log M_{\text{sub}}$ when using Equation (40) for M_{acc} and M_{peak} .

$$\log(M_{\text{cut}}(z)) = M_0 + M_1 z + M_2 z^2 + M_3 z^3 + M_4 z^4. \quad (36)$$

4.3 Number of subhalos as a function of their host halo mass

Characterizing the number of subhalos in hosts of different masses M_{vir} is relevant for several reasons. The predicted abundance of satellites in Milky Way mass galaxies has been a very active topic since N -body numerical simulations could resolve subhalos in galactic halos (Klypin et al. 1999b; Moore et al. 1999). Subhalos are the natural sites for satellite galaxies, thus, using statistical approaches that connect the stellar mass of central/satellite galaxies to dark matter halos/subhalos allows prediction of the abundance of satellite galaxies as function of the stellar mass of their host. Previous studies have used these predictions in order to make direct comparisons to what is observed from large galaxy groups catalogues (Yang, Mo & van den Bosch 2009; Rodríguez-Puebla, Drory & Avila-Reese 2012;

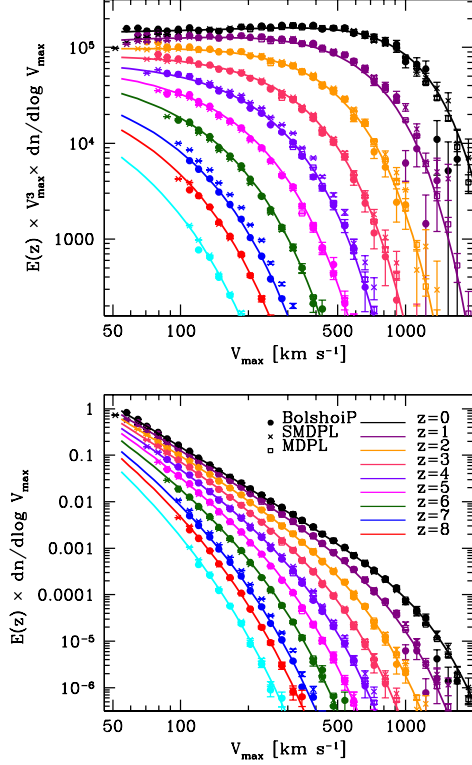


Figure 14. Maximum circular velocity function of distinct halos from $z = 0$ to $z = 9$. The different solid lines show the fits to the simulation, Equation (41). **Upper Panel:** The product $E(z) \times V_{\max}^3 \times dn_h/d\log V_{\max}$ is shown, to split the evolution of the velocity function. **Bottom Panel:** Same but for the product $E(z) \times dn_h/d\log V_{\max}$.

Rodríguez-Puebla, Avila-Reese & Drory 2013a, and reference therein). These studies have found that in order to reconcile the observed abundance of satellite galaxies in clusters of different masses, the galaxy stellar-to-halo mass relation of central and satellite galaxies should be different, especially at lower masses (see also, Neistein et al. 2011; Wetzel et al. 2013).

Figure 12 shows the mean cumulative number of subhalos for various host halos with masses $M_{\text{vir}} = 10^{11}, 10^{12}, 10^{13}$, and $10^{14} M_{\odot}$, solid lines. In the left panel of this figure we present the results when defining subhalo mass at the time when they first became subhalos, i.e., at their time of first accretion, M_{acc} . The right panel of the same figure presents the results when defining the mass of subhalos when they reached the maximum mass over their main branch, M_{peak} .

Following Boylan-Kolchin et al. (2010), in this paper we parametrise the mean cumulative number of subhalos at a given host halo mass, M_{vir} , as

$$\langle N_{\text{sub}}(> M_{\text{sub}} | M_{\text{vir}}) \rangle = \mu_0 \left(\frac{\mu}{\mu_1} \right)^a \exp \left[- \left(\frac{\mu}{\mu_{\text{cut}}} \right)^b \right], \quad (37)$$

$$\mu_0 = (M_{\text{vir},12})^c \quad (38)$$

where $\mu = M_{\text{sub}}/M_{\text{vir}}$ and μ_0 is a normalisation term that depends on M_{vir} . We use the above functional form for both

M_{acc} and M_{peak} . For M_{acc} we find that $a = -0.777$, $b = 1.210$, $\mu_1 = 0.030$, $\mu_{\text{cut}} = 0.199$ and $c = 0.102$. For M_{peak} we find that $a = -0.749$, $b = 1.088$, $\mu_1 = 0.042$, $\mu_{\text{cut}} = 0.199$ and $c = 0.118$.

It is interesting to see the consistency of Equation (37) with the values reported in the literature based on the spatial clustering of galaxies. Previous studies have concluded that the mean occupation number of satellite galaxies above some stellar mass M_* increases roughly proportionally to halo mass, i.e., $N_{\text{sat}} \propto M_{\text{vir}}$ (see, e.g., Zehavi et al. 2005, 2011). A recent study to redshift $z = 1.2$ (Skibba et al. 2015) found $N_{\text{sat}} \propto M_{\text{vir}}^\alpha$ with favored values of $\alpha \approx 0.95$ to 1.2. Ignoring the exponential term in Equation (37) for $M_{\text{sub}} \lesssim 0.1 M_{\text{vir}}$, we find that mean occupation number of subhalos (above some mass M_{sub}) is $N_{\text{sub}} \propto M_{\text{vir}}^{c-a} \approx M_{\text{vir}}^{0.9}$, which is consistent with observations.

Note that in Equation (37) the parameter μ_1 gives the typical fractional mass of the most massive subhalo relative to the host halo M_{vir} for Milky Way sized halos (i.e., $M_{\text{vir}} \sim 10^{12} h^{-1} M_{\odot}$), and thus $\mu_1 \times M_{\text{vir}}$ gives the typical mass of the most massive subhalo. When defining subhalo masses at the time of their first accretion, we find that the typical mass of the most massive subhalo is $\sim 3\%$ of its host halo mass. For Milky Way mass halos, the most massive subhalo typically has a mass of $M_{\text{acc}} \sim 3 \times 10^{10} h^{-1} M_{\odot}$, which corresponds to a stellar mass of $\sim 10^{7.9} M_{\odot}$ based on abundance matching results. This is more than an order of magnitude lower than the LMC. When defining subhalo masses as M_{peak} , we find that the typical mass of the most massive subhalo is $\sim 4\%$ of its host halo, which is also more than an order of magnitude less than the LMC. Indeed, only a small fraction of Milky Way mass galaxies have a satellite as massive as the LMC (Busha et al. 2011; Rodríguez-Puebla, Avila-Reese & Drory 2013b), which has a total mass $\sim 10^{11} M_{\odot}$ (e.g., Besla 2015) including its dark matter halo.

Note that the number of subhalos of mass between $\log M_{\text{sub}}$ and $\log M_{\text{sub}} + d\log M_{\text{sub}}$ residing in halos of mass M_{vir} , usually referred as the conditional subhalo mass function, can be obtained by simply differentiating $\langle N_{\text{sub}}(> M_{\text{sub}} | M_{\text{vir}}) \rangle$

$$\Phi_{\text{sub}}(M_{\text{sub}} | M_{\text{vir}}) = \frac{d\langle N_{\text{sub}}(> M_{\text{sub}} | M_{\text{vir}}) \rangle}{d\log M_{\text{sub}}}. \quad (39)$$

We can therefore use this definition to infer the subhalo mass function:

$$\frac{dn_{\text{sub}}}{d\log M_{\text{sub}}} = \int \Phi_{\text{sub}}(M_{\text{sub}} | M_{\text{vir}}) \frac{dn_h}{d\log M_{\text{vir}}} d\log M_{\text{vir}}. \quad (40)$$

Figure 13 shows the comparison between the measured subhalo mass function from the BolshoiP, SMDPL and MDPL simulations and by computing $dn_{\text{sub}}/d\log M_{\text{sub}}$ when using Equation (40) both for M_{acc} and M_{peak} . We find that Equation (40) provides an accurate prescription for the subhalo mass function.

5 HALO AND SUBHALO VELOCITY FUNCTION

The comoving number density of distinct halos with maximum circular velocity between $\log V_{\max}$ and $\log V_{\max} + d\log V_{\max}$ —i.e., the maximum circular velocity function ($dn_h/d\log V_{\max}$)—is recognized as a sensitive probe

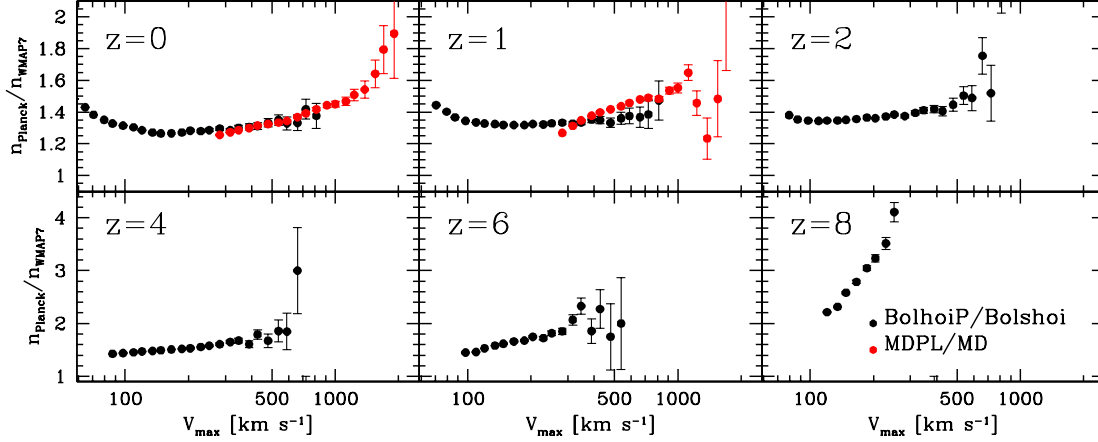


Figure 15. The ratio of the distinct halo number densities between the Bolshoi-Planck n_{BP} and the Bolshoi n_B simulations as a function of V_{\max} at $z = 0, 1, 2, 4, 6$ and $z = 8$.

Table 5. Best fit parameters for Equation (42).

χ_i	$\chi_{0,i}$	$\chi_{1,i}$	$\chi_{2,i}$
$A/E(z)$	4.785	-0.207	0.011
a	-1.120	0.394	-0.306
b	1.883	-0.146	0.005
$\log V_0$	2.941	-0.169	0.002

of dark matter (Cole & Kaiser 1989; Shimasaku 1993; Gonzalez et al. 2000; Zavala et al. 2009; Papastergis et al. 2011; Trujillo-Gomez et al. 2011; Schneider et al. 2014; Klypin et al. 2015; Papastergis et al. 2015). Figure 14 shows the maximum circular velocity function $dn_h/d \log V_{\max}$ from $z = 0$ to $z = 8$ for the Bolshoi-Planck and MD-Planck simulations. The upper panel of this figure shows the product $E(z) \times V_{\max}^3 \times dn_h/d \log V_{\max}$ while the bottom panel shows the product $E(z) \times dn_h/d \log V_{\max}$. Recall that $E(z)$ is the expansion rate, Equation (4).

In this paper we parametrize the velocity function as

$$\frac{dn_h}{dV_{\max}} = AV_{\max}^2 \left[\left(\frac{V_{\max}}{V_0} \right)^{-a} + 1 \right] \exp \left[- \left(\frac{V_{\max}}{V_0} \right)^{-b} \right]. \quad (41)$$

We assume the following redshift dependence for the parameters $\chi_i = A/E(z)$, a , b and $\log V_0$

$$\chi_i = \chi_{0,i} + \chi_{1,i}z + \chi_{2,i}z^2. \quad (42)$$

Table 5 lists the best fit parameters for the velocity function.

Figure 15 shows the ratio of the number densities of distinct halos between the Bolshoi-Planck, n_{BP} , and the Bolshoi n_B simulations as a function of V_{\max} at $z = 0, 1, 2, 4, 6$ and $z = 8$. At $z = 0$, on average, there are $\sim 25\%$ more halos with $V_{\max} = 200$ km/s in the Bolshoi-Planck than in the Bolshoi simulation, and this stays practically constant

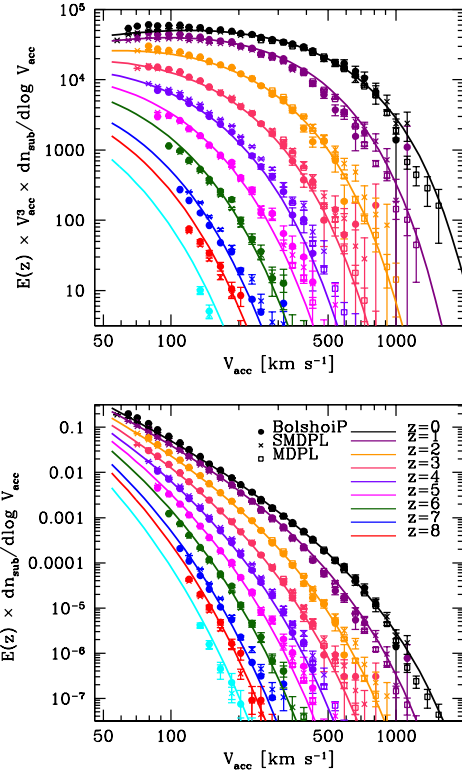


Figure 16. Redshift evolution of the subhalo maximum circular velocity function, with circular velocity V_{acc} measured at accretion.

for most V_{\max} values up to $z = 2$. This fraction increases at $z = 4, 6$ and more drastically at $z = 8$ where we find that there are $\sim 60, 78$ and 258% more $V_{\max} = 200$ km/s halos in the Bolshoi-Planck than in the Bolshoi simulation.

Figure 16 shows the redshift evolution of the subhalo

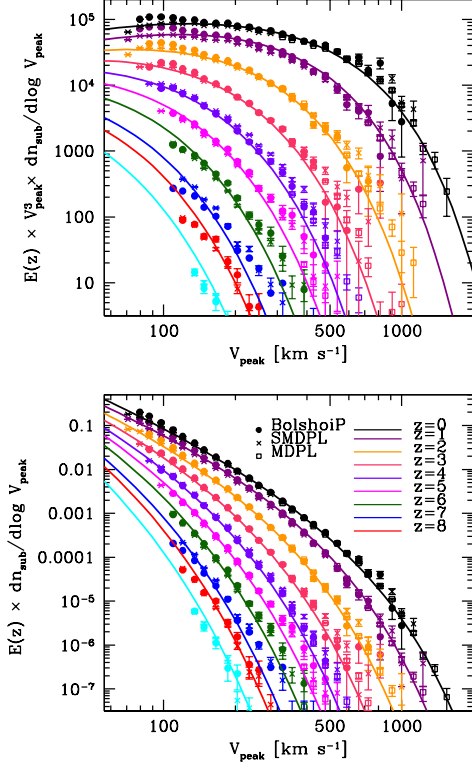


Figure 17. Redshift evolution of the subhalo circular velocity function, as a function of the subhalo's peak circular velocity V_{peak} .

Table 6. Best fit parameters to the subhalo maximum circular velocity function.

Parameter	V_{acc}	V_{peak}
C_0	-0.6768	-0.5600
C_1	1.3098	1.5905
C_2	-1.1288	-1.1360
C_3	0.0090	-0.0378
C_4	0.214820	0.18092
$\alpha_{\text{sub},1}$	1.1375	1.1583
$\alpha_{\text{sub},1}$	0.5200	0.5806
V_0	0.2595	0.5410
V_1	3.5144	3.4335
V_2	-2.8817	-3.0026
V_3	-0.3910	-0.3687
V_4	0.8729	0.9450

maximum circular velocity function, $dn_{\text{sub}}/d\log V_{\text{sub}}$, at the time at the time of their accretion, V_{acc} . Similarly, Figure 17 shows $dn_{\text{sub}}/d\log V_{\text{sub}}$ for V_{peak} . Recall that V_{peak} is defined as the maximum circular velocity reached along the main progenitor assembly. Reddick et al. (2013) found that V_{peak} is a better proxy for galaxy stellar mass/luminosity than alternatives such as V_{acc} or M_{peak} . The solid lines in Figures 16 and 17 show the best fits to $dn_{\text{sub}}/d\log V_{\text{sub}}$. We motivate the fitting functional form for $dn_{\text{sub}}/d\log V_{\text{sub}}$ using the same arguments as for $dn_{\text{sub}}/d\log M_{\text{sub}}$. As we will show later, the mean number of subhalos above some maximum circular velocity is nearly independent of host maximum velocity. To be specific, we parameterize $dn_{\text{sub}}/d\log V_{\text{sub}}$ using the following functional form:

$$\frac{dn_{\text{sub}}}{d\log V_{\text{sub}}} = C_{\text{sub}}(z)G(V_{\text{sub}}, z)\frac{dn_{\text{h}}}{d\log V_{\text{max}}}, \quad (43)$$

where

$$\log C_{\text{sub}}(z) = C_0 + C_1 a + C_2 a^2 + C_3 a^3 + C_4 a^4, \quad (44)$$

and

$$G(M_{\text{vir}}, z) = X^{\alpha_{\text{sub},1}} \exp(-X^{\alpha_{\text{sub},2}}), \quad (45)$$

where $X = V_{\text{max}}/V_{\text{cut}}(z)$. The function fit form for $V_{\text{cut}}(z)$ is given by

$$\log(V_{\text{cut}}(z)) = V_0 + V_1 z + V_2 z^2 + V_3 z^3 + V_4 z^4. \quad (46)$$

Figure 18 shows the mean cumulative number of subhalos of maximum circular velocity V_{sub} for various host halos with maximum circular velocities $V_{\text{max}} = 200, 500, 1000$ and $V_{\text{max}} = 1580$ km/s for the BolshoiP, SMDPL and MDPL simulations (dashed, solid and long dashed lines respectively). In the left panel of this figure we present the results when defining $V_{\text{sub}} = V_{\text{acc}}$. The right panel of the same figure presents the results when defining $V_{\text{sub}} = V_{\text{peak}}$. Analogously to the mean cumulative number of subhalos at a given host halo mass, $\langle N_{\text{sub}}(> M_{\text{sub}}|M_{\text{vir}}) \rangle$, we parameterize the mean cumulative number of subhalos above some maximum circular velocity at a given host halo maximum circular velocity as:

$$\langle N_{\text{sub}}(> V_{\text{sub}}|V_{\text{max}}) \rangle = \left(\frac{\mu}{\mu_1}\right)^a \exp\left[-\left(\frac{\mu}{\mu_{\text{cut}}}\right)^b\right], \quad (47)$$

where $\mu = V_{\text{sub}}/V_{\text{max}}$. We use the above functional form for both V_{acc} and V_{peak} . The resulting best fitting parameters when using V_{acc} are $a = -3.0881$, $b = 7.545$, $\mu_1 = 0.356$ and $\mu_{\text{cut}} = 0.736$, while for V_{peak} are $a = -3.045$, $b = 8.850$, $\mu_1 = 0.416$ and $\mu_{\text{cut}} = 0.738$. Similarly to Equation (37), the parameter μ_1 in Equation (47) gives the typical fractional maximum circular velocity of the most massive subhalo relative to the host halo. For host halos with velocities of ~ 200 km/s (MW-sized halo) the typical most massive subhalo has a velocity of $V_{\text{acc}} \sim 71.2$ km/s and of $V_{\text{peak}} \sim 83.2$ km/s. These values are more consistent with the velocity of the LMC. See also Busha et al. (2011) which compared the number of satellites as massive as the LMC/SMC in the Bolshoi simulation with the number observed in MW-size galaxies in SDSS.

The number of subhalos of maximum circular velocity between $\log V_{\text{sub}}$ and $\log V_{\text{sub}} + d\log V_{\text{sub}}$ residing in halos of maximum circular velocity V_{max} , referred as the conditional subhalo maximum circular velocity function, is given by

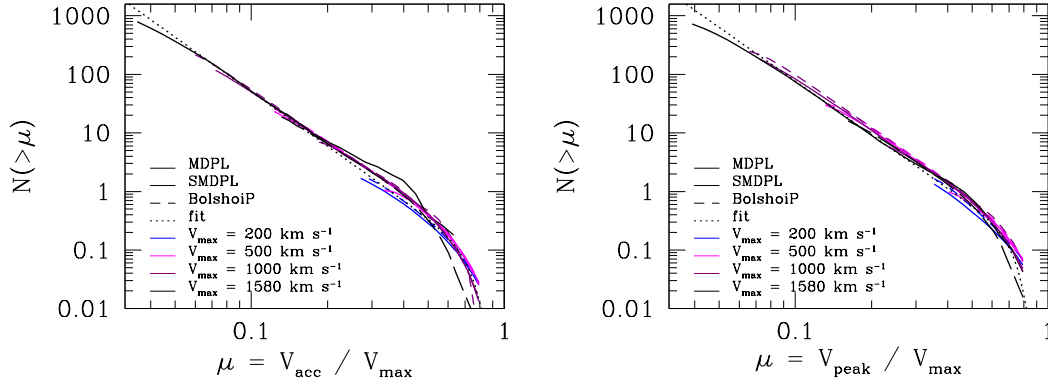


Figure 18. Mean cumulative number of subhalos of maximum circular velocity V_{sub} for host halos with maximum velocities $V_{\text{max}} = 200, 500, 1000$ and 1580 km/s as a function of $V_{\text{sub}}/V_{\text{max}}$ for (left panel) $V_{\text{sub}} = V_{\text{acc}}$, and (right panel) $V_{\text{sub}} = V_{\text{peak}}$. The dotted curve is the fitting function Equation (47).

$$\Phi_{\text{sub}}(V_{\text{sub}}|V_{\text{max}}) = \frac{d\langle N_{\text{sub}}(> V_{\text{sub}}|V_{\text{max}}) \rangle}{d \log V_{\text{sub}}}. \quad (48)$$

Using this definition we can thus derive the maximum circular velocity function as:

$$\frac{dn_{\text{sub}}}{d \log V_{\text{sub}}} = \int \Phi_{\text{sub}}(V_{\text{sub}}|V_{\text{max}}) \frac{dn_{\text{h}}}{d \log V_{\text{max}}} d \log V_{\text{max}}. \quad (49)$$

6 HALO CONCENTRATION AND SPIN

6.1 Halo concentrations

High resolution N -body simulations have shown that the density profile of dark matter halos can be well described by the Navarro, Frenk & White (1996, NFW) profile,

$$\rho_{\text{NFW}}(r) = \frac{4\rho_s}{(r/R_s)(1+r/R_s)^2}. \quad (50)$$

The scale radius R_s is the radius where the logarithmic slope of the density profile is -2 . The NFW profile is completely characterized by two parameters, for example ρ_s and R_s , or more usefully the halo mass, M_{vir} , and its concentration parameter, c_{vir} . The concentration parameter is defined as the ratio between the virial radius R_{vir} and the scale radius R_s :

$$c_{\text{vir}} = \frac{R_{\text{vir}}}{R_s}. \quad (51)$$

Figure 19 shows halo concentrations, c_{vir} , as a function of M_{vir} for redshifts $z = 0, 1, 2, 4$, and 6 . The left panel of the figure shows halo concentrations calculated by finding the best scale radius, R_s assuming a NFW profile for each halo in the simulation. Instead, the right panel shows halo concentrations calculated by determining the scale radius, R_s using the V_{max} and M_{vir} relationship from the NFW formulae, see Klypin, Trujillo-Gomez & Primack (2011) and Klypin et al. (2014); (see also, Behroozi, Wechsler & Wu 2013). For the NFW profile, the radius at which the circular velocity is maximized is $R_{\text{max}} = 2.1626 R_s$ (Klypin et al. 2001; Behroozi, Wechsler & Wu 2013), and it can be shown that

$$\frac{c_{\text{vir}}}{f(c_{\text{vir}})} = V_{\text{max}}^2 \frac{R_{\text{vir}}}{GM_{\text{vir}}} \frac{2.1626}{f(2.1626)} \quad (52)$$

where

$$f(x) \equiv \ln(1+x) - \frac{x}{1+x}. \quad (53)$$

The Klypin concentration $c_{\text{vir,K}}$ can be found by solving Equation (52) numerically. It is more robust than determining R_s by fitting the NFW profile, especially for halos with few particles, since halo profiles are not well determined both at distances comparable to the simulation force resolution and also at large distances near R_{vir} . Figure 19 shows that at high redshifts NFW concentrations are systematically lower than Klypin concentrations. Fitting functions for $c_{\text{vir,K}}$ are given in Klypin et al. (2014) for all halos and for relaxed halos, for both Bolshoi-Planck/MultiDark-Planck and Bolshoi/MultiDark simulations; fitting functions are also given there for concentrations of halos defined by the 200c overdensity criterion. Key processes that drive the evolution of halo concentration are also discussed there. Diemer & Kravtsov (2015) discusses the relation between halo concentration, the slope of the fluctuation power spectrum and the peak height.

The solid lines in the left panel of Figure 19 show the resulting Klypin concentrations by solving Equation (52) and using the best fitting values for the $V_{\text{max}} - M_{\text{vir}}$ relation from Section 3.1, see Equation (5). At $z = 0$ and $z = 1$ the resulting concentrations are in very good agreement with what is found in the simulation with an accuracy of $\sim 3\%$ for halos above $M_{\text{vir}} = 10^{10} h^{-1} M_{\odot}$. However, at higher redshifts $z = 2, 4, 6$, our predicted Klypin concentrations have an accuracy of $\sim 10\%$.

6.2 Halo Spin

The left panel of Figure 20 shows the medians for the spin parameter λ_{P} as a function of M_{vir} at $z = 0, 2, 4, 6$, and 8 . The spin parameter for every halo in the simulations was calculated using the definition (Peebles 1969):

$$\lambda_{\text{P}} = \frac{J|E|^{1/2}}{GM_{\text{vir}}^{5/2}}, \quad (54)$$

where J and E are the total angular momentum and the total energy of a halo of mass M_{vir} . As others have found,

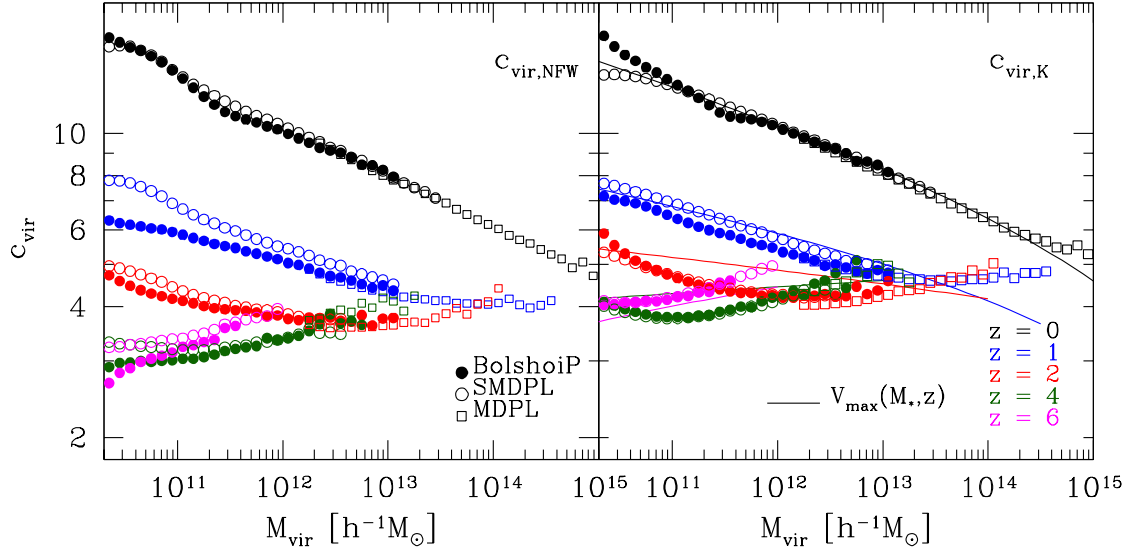


Figure 19. Halo concentration as a function of M_{vir} at $z = 0, 1, 2, 4$, and 6 . The left panel in the figure shows halo concentrations calculated by finding the scale radius, R_s assuming a NFW profile in the simulation. Instead, the right panel shows Klypin halo concentrations from determining the scale radius, R_s using the V_{max} and M_{vir} relationship from the NFW formulae (see text). Solid lines in the left panel show the resulting Klypin concentrations by solving Equation (52) and using the best fitting values for the $V_{\text{max}} - M_{\text{vir}}$ relation from Section 3.1.

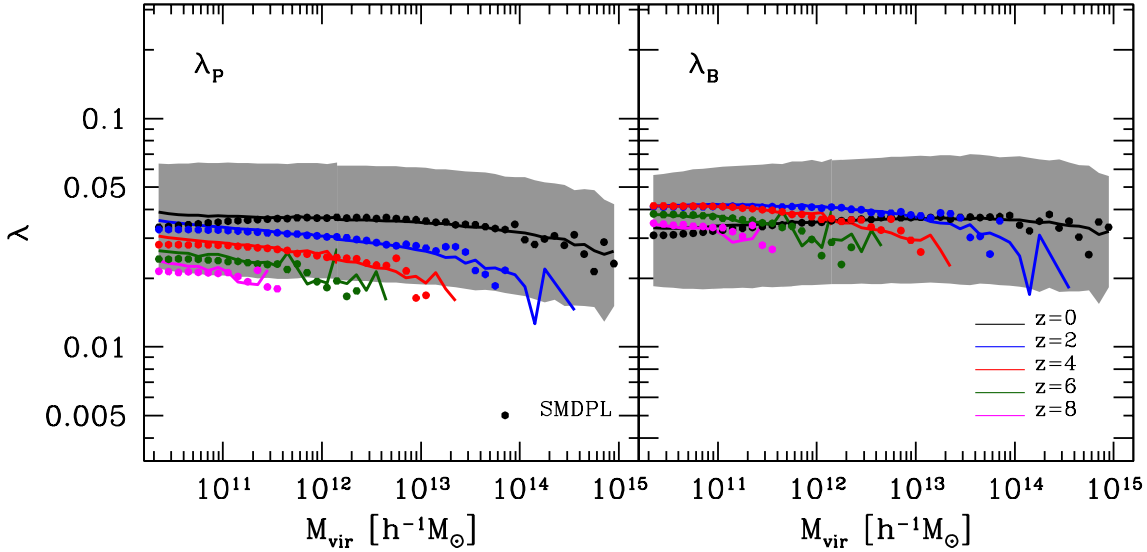


Figure 20. Spin parameter as a function of M_{vir} at $z = 0, 2, 4, 6$, and 8 . Medians are shown as the solid lines. At $z = 0$ the grey area is the 68% range of the distribution. The left panel of this figure shows the spin parameter calculated using Equation (54) while the right panel shows the spin parameter calculated using Equation (55).

Table 8. Best fit parameters to Schechter-like distribution function for $P(\log \lambda)d\log \lambda$.

Simulation	α_P	β_P	$\log \lambda_{0,P}$	α_B	β_B	$\log \lambda_{0,B}$
BolshoiP	4.126	0.610	-2.919	3.488	0.6042	-2.878
SMDPL	4.090	0.612	-2.917	4.121	0.611	-2.916
MDPL	4.047	0.612	-2.914	3.468	0.591	-2.907

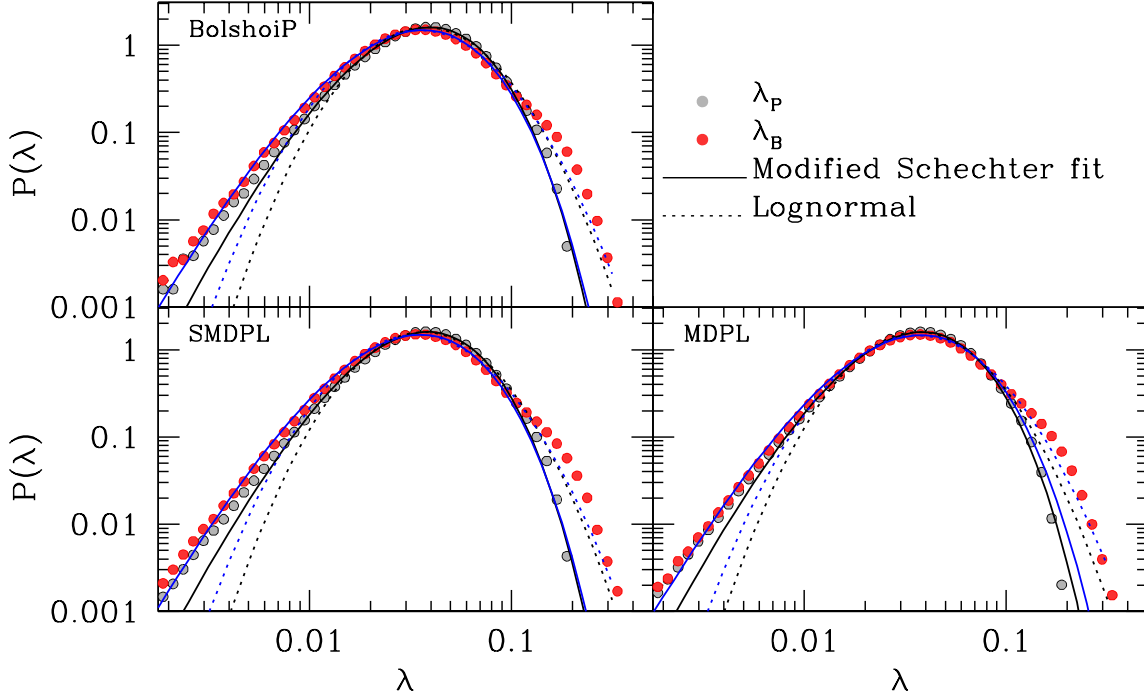


Figure 21. Halo spin distribution for the BolshoiP (upper left), SMDPL (bottom left) and MDPL (bottom right) simulations. Filled grey circles show the λ_P distribution while the red circles show the λ_B distribution. Solid lines show the best fit to a Schechter-like function, Equation (57), while the dotted lines show the best fit for a lognormal distribution, Equation (56). The black (blue) lines are the best fits to the λ_B (λ_P) distributions. Both distributions are well fit at low values by the Schechter-like distribution, which also is a good fit the the λ_P distribution at higher values, while λ_B is somewhat better fit by a log-normal distribution at higher values.

Table 7. Best fit parameters to the lognormal distribution function $P(\log \lambda)d \log \lambda$.

Simulation	σ_P	$\log \lambda_{0,P}$	σ_B	$\log \lambda_{0,B}$
BolshoiP	0.248	-1.423	0.268	-1.459
SMDPL	0.249	-1.435	0.268	-1.471
MDPL	0.250	-1.438	0.271	-1.443

the spin parameter λ_P correlates only weakly with halo mass especially at $z = 0$. The median value for Milky Way mass halos (i.e., with $M_{\text{vir}} \sim 10^{12} h^{-1} M_\odot$) at $z = 0$ is $\lambda_P \sim 0.036$, and it decreases a factor of ~ 1.8 at $z = 6$, that is, $\lambda_P \sim 0.02$. For Milky Way mass halos, the dispersion is approximately ~ 0.24 dex at $z = 0$ and it decreases to ~ 0.16 dex at $z = 6$. Note that the dispersion is not symmetric, meaning that the distribution of λ_P is not a lognormal distribution. This is consistent with previous findings based on high resolution N -body simulations (e.g., Bett et al. 2007).

The right panel of Figure 20 shows the spin distribution calculated using the alternative definition (Bullock et al. 2001a):

$$\lambda_B = \frac{J}{\sqrt{2} M_{\text{vir}} V_{\text{vir}} R_{\text{vir}}}, \quad (55)$$

which can be obtained from Equation (54) by assuming all particles to be in circular orbits. Similarly to λ_P , the spin parameter λ_B correlates only weakly with halo mass especially at $z = 0$. We found that the median value for Milky Way mass halos at $z = 0$ is $\lambda_P \sim 0.035$ and it decreases to $\lambda_P \sim 0.027$ at $z = 6$. For Milky Way mass halos, the dispersion of λ_B is slightly larger than of λ_P ; we find that it is ~ 0.27 dex at $z = 0$ and it decreases to ~ 0.2 dex at $z = 6$.

The spin parameter λ_B slightly increases at high redshifts especially for low mass halos, $M_{\text{vir}} \lesssim 10^{12} M_\odot$. In contrast, the value of the spin parameter λ_P shows a systematic decrease as redshift increases. This was previously noted over the interval $z = 0 - 2$ by Hetzner & Burkert (2006), who attribute the different evolution of the two spin parameters mainly to different effects of minor mergers on λ_P and λ_B .

Figure 21 quantifies in more detail the distribution of halo spins separately for the BolshoiP, SMDPL and MDPL simulations. In order to avoid resolution effects and to obtain reliable statistics, we calculate the distribution of halo spins in the halo mass range $10^{11} - 10^{14} h^{-1} M_\odot$ for the BolshoiP (upper left panel) and SMDPL (bottom left panel) simulations, while for the MDPL (bottom right panel) simulation we do the same but for the mass range $10^{12} - 10^{14} h^{-1} M_\odot$. In all the panels the grey filled circles show the distribution for λ_P while the red filled circles show the distribution for λ_B . As anticipated from the $\lambda - M_{\text{vir}}$ relationship, the log λ distributions are asymmetrical. This is more evident for λ_P

than for λ_B . In order to quantify this we try to fit all the distributions using a lognormal probability distribution:

$$P(\log \lambda) = \frac{1}{\sqrt{2\pi\sigma^2}} \exp\left(-\frac{\log^2(\lambda/\lambda_0)}{2\sigma^2}\right). \quad (56)$$

The best fit parameters of $P(\log \lambda)$ both for λ_P and for λ_B are listed in Table 7. We find that while the lognormal distribution gives a fairly good description for $P(\log \lambda_B)$ this is not the case for $P(\log \lambda_P)$ for all the simulations. In particular, the distribution has too many halos with low values of λ_P . In order to provide a more accurate description of the halo distribution we propose to use a Schechter-like function given by

$$P(\log \lambda) = Af(\lambda), \quad (57)$$

where

$$f(\lambda) = \left(\frac{\lambda}{\lambda_0}\right)^{-\alpha} \exp\left[-\left(\frac{\lambda}{\lambda_0}\right)^\beta\right], \quad (58)$$

$$A = \left[\int_{-\infty}^{\infty} f(\lambda) d\lambda\right]^{-1}. \quad (59)$$

The best fit parameters for BolshoiP, SMDPL and MDPL simulations for both λ_P and λ_B are listed in Table 7 for the log-normal distribution and Table 8 for the Schechter-like distribution. We find that a Schechter-like function gives a more accurate prescription for the distribution of λ_P than for λ_B . In particular, this distribution has some problems in reproducing the tail of high λ_B that declines more like a lognormal distribution.

It is thought that the angular momentum of galaxies is related the angular momentum of dark matter halos and thus to their spin parameter. Under this assumption, the scale length of disk galaxies, R_d , can be obtained in terms of λ and R_{vir} . Specifically the relation is given by $R_d \propto \lambda \times R_{\text{vir}} \propto \lambda \times M_{\text{vir}}^{1/3}$. As before, if we assume for simplicity that the M_b/M_{vir} ratio is constant, the relation between a galaxy's radius and its baryonic mass is given by $R_d \propto \lambda \times M_b^{1/3}$. Note that the scatter of the size-mass relation is just the resulting scatter of the $\lambda - M_{\text{vir}}$ relation. Indeed, the dispersion of the spin parameter, either λ_P or λ_B , is very similar to the observed dispersion of disk galaxy scale lengths at least at low redshifts where reliable measurements can be obtained (see e.g., Mosleh, Williams & Franx 2013).

Note that the different redshift evolution of the $\lambda_P - M_{\text{vir}}$ and $\lambda_B - M_{\text{vir}}$ relations leads to different predictions of the $R_d - M_b$ relation and its evolution. In particular, models of galaxy formation calculating galaxy sizes based on the spin parameter λ_B will result in more extended galaxies (and potentially in larger numbers of low surface brightness galaxies) at high redshifts compared to those models using λ_P . Is also possible that galaxy star formation rates could be affected since more extended galaxies presumably have lower gas surface densities than more compact disks, and thus lower SFRs according to the Kennicutt-Schmidt law.

Two recent papers have discussed the evolution of galaxy sizes out to redshift $z \sim 8$ using Hubble Space Telescope images, mainly from the CANDELS survey. Shibuya, Ouchi & Harikane (2015) finds that the median effective radius r_e evolves with redshift as $r_e \propto (1+z)^{-1.3}$, with no evolution in the slope, the median Sérsic index ($n \sim 1.5$), or the standard deviation of the log-normal

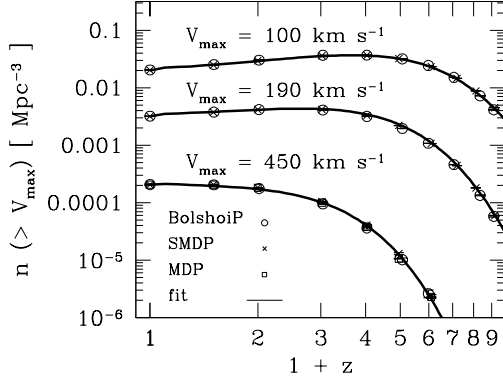


Figure 22. Evolution of the velocity function V_{max} for fixed $V_{\text{max}} = 100, 190$ and 450 km/s for the BolshoiP, SMDPL, and MDPL simulations. The solid lines are the fits to Equation (41). For low velocities the velocity function is practically constant after redshift $z \sim 4$, while for high velocity halos it is nearly constant after redshift $z \sim 1$.

distribution. They find that the ratio of the effective radius to the virial radius of the halos is nearly constant at $r_e/R_{\text{vir}} = 0.01 - 0.035$. This is just what one would expect from the lack of redshift evolution in λ_B , while the factor of ~ 2 decline in λ_P from $z = 0$ to 8 would predict a corresponding decline in the ratio r_e/R_{vir} . The other recent paper, Curtis-Lake et al. (2014), finds a slower decline of effective radius with redshift, and in fact cannot reject the possibility that there is no size evolution. This is possibly consistent with the modest increase with redshift of λ_B for lower mass halos, and inconsistent with the expected decrease in r_e/R_{vir} from the decline in λ_P . The radii of these high-redshift galaxies are being measured in rest-frame UV, which is typically rather clumpy (Shibuya et al. 2015; Curtis-Lake et al. 2014). It will be very interesting to see what sort of galaxy size evolution with higher redshifts is revealed by James Webb Space Telescope at rest-frame optical wavelengths.

7 ON THE EVOLUTION OF $V_{\text{max}} - M_*$

Early determinations of the evolution in the maximum circular velocity and the stellar mass/luminosity relations—the Tully-Fisher relation for spiral galaxies and the Faber-Jackson relation for ellipticals—have found only a weak evolution from $z \sim 0.85$ to $z \sim 0$ (Conselice et al. 2005). This result has been further supported and generalized in Kassin et al. (2007) from $z \sim 1$ to $z \sim 0$, based on fairly large samples of galaxies from AEGIS and DEEP2 and adopting the indicator $S_{0.5}^2 = 0.5V_{\text{max}}^2 + \sigma_g^2$ which accounts for disordered motions (Weiner et al. 2006; Covington et al. 2010). On the other hand, observations indicate that at $z \lesssim 1.5$ the number density of star forming galaxies at a fixed velocity evolves very little, while the number density of quiescent galaxies evolves more rapidly (e.g., Bezanson, van Dokkum & Franx 2012).

Figure 22 shows that the comoving number density of

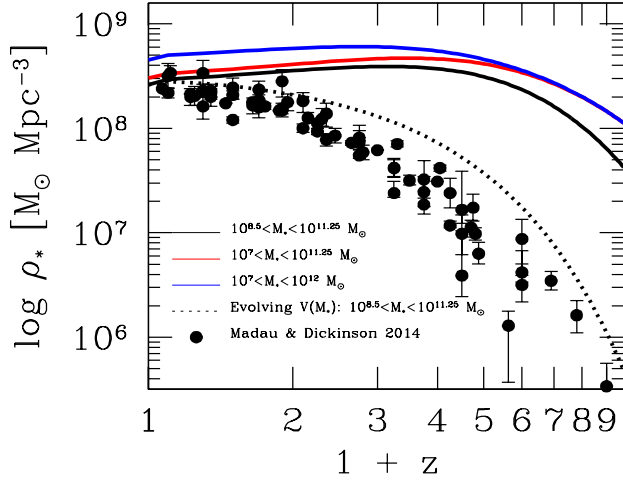


Figure 23. Cosmic stellar mass density since $z \sim 9$. Filled circles show the observations compiled in Madau & Dickinson (2014). The solid curves show the predicted cosmic stellar mass density using fits to the Tully-Fisher and Faber-Jackson velocity-to-stellar-mass relations as described in the text, assuming that these relations are independent of redshift and that the V_{\max} of dark matter halos is the same as the $V_{\max,g}$ of galaxies. The solid black line shows the predicted cosmic stellar mass density for a range of stellar masses $\log(M_*/M_\odot) = 8.5 - 11.25$. Comparing the red curve, for $\log(M_*/M_\odot) = 7 - 11.25$, to the black curve shows that including lower stellar masses increases ρ_* more at high redshifts; comparing the blue curve, for $\log(M_*/M_\odot) = 7 - 12$, to the black and red curves shows that including higher stellar masses increases ρ_* more at low redshifts. Clearly, all of these predictions are inconsistent with observations at $z \gtrsim 1$ —they produce too much stellar mass density at early redshifts, and the wider stellar mass range represented by the blue curve exceeds the observed stellar mass density even at $z = 0$. Since the stellar mass function is evolving, velocity-mass relations like Tully-Fisher must also evolve. The dotted lines show the predictions when using a model in which the maximum circular velocity-to-stellar mass relation evolves with redshift as described in the text.

low circular velocity halos is nearly constant since $z \sim 4$ but high mass/velocity halos have more evolution. Halos of a given circular velocity at high redshift are lower in mass but denser than halos of the same circular velocity at lower redshift. To what extent is the nearly constant comoving number density of halos as a function of their circular velocity consistent with the weak evolution of the Tully-Fisher relation? This is particularly interesting if the galaxy stellar mass function evolves with redshift, as was first pointed out in Bullock et al. (2001b).

In this section we investigate the above question assuming that the Tully-Fisher and Faber-Jackson relations do not evolve with redshift and that there is a one-to-one correspondence between the maximum circular velocity of halos and galaxies, i.e., $V_{\max} = V_{\max,g}$. To do so, our first step is to convert the Tully-Fisher and Faber-Jackson relations into circular velocities. Arguments based on the Jeans equation in virialized systems result in the relation $V_c = K\sigma$, where typical values for K are $\sqrt{2} - \sqrt{3}$ (Binney & Tremaine 2008). While there is an extensive discussion in the literature of what is the right value for K , following Dutton et al. (2011) here we assume that $K = 1.54$ which is a value halfway

between different groups. The next step is to derive an average maximum circular velocity-to-stellar mass relation for all galaxies: $\langle \log V_{\max,g} \rangle = \langle \log V_{\max,g} \rangle (\log M_*)$. The method is to use the average Tully-Fisher and Faber-Jackson relations for local galaxies and take into account the observed fraction of disk and elliptical galaxies. For simplicity, we assume that all disk galaxies are star-forming systems while ellipticals correspond to quiescent galaxies. Then the average maximum circular velocity is given by

$$\langle \log V_{\max,g} \rangle = f_{\text{SF}} \langle \log V_{\max,\text{TF}} \rangle + f_{\text{Q}} \langle \log V_{\max,\text{FJ}} \rangle. \quad (60)$$

where $\langle \log V_{\max,\text{FJ}} \rangle = \langle \log(1.54\sigma) \rangle$ and $f_{\text{SF}} = 1 - f_{\text{Q}}$. Note that the above equation depends on stellar mass. We take the fraction of quiescent galaxies f_{Q} from Behroozi, Wechsler & Conroy (2013b), and we use the fits for the Tully-Fisher and Faber-Jackson relations reported in Dutton et al. (2011). The fraction of quiescent galaxies f_{Q} has been taken from Behroozi, Wechsler & Conroy (2013b). We assume for simplicity that the maximum circular velocity of dark matter halos, V_{\max} , corresponds to the maximum circular velocity of galaxies, $V_{\max,g}$, i.e., $V_{\max} = V_{\max,g}$. In this way, we can then solve Equation (60), $\langle \log V_{\max,g} \rangle = \langle \log V_{\max,g} \rangle (\log M_*)$, for M_* and thus transform velocities into stellar mass.

The black solid line in Figure 23 shows the predicted cosmic stellar mass density for galaxies with stellar mass $M_* = 10^{8.5} - 10^{11.25} M_\odot$ since $z = 9$ assuming that $\langle \log V_{\max,g} \rangle (\log M_*)$ is independent of redshift, and the red and blue curves are the same for wider ranges of stellar masses. For comparison, we plot a recent compilation from Madau & Dickinson (2014) of the evolution of the observed stellar mass density. Our simple model represented by the black curve seems to be roughly consistent with the observational evidence of the weak evolution of the maximum circular velocity since $z \sim 1$. In contrast, at high redshifts the model produces far too many stars. We thus conclude that a strong evolution of the Tully-Fisher and Faber-Jackson relations is required to higher redshifts in order to reconcile the predicted cosmic stellar mass density with observations.

Based only on theoretical arguments, is it possible to derive a simple model for the redshift evolution for $\langle \log V_{\max,g} \rangle (\log M_*)$? In Section 3.1, we found that the evolution of the maximum circular velocity of dark matter halos is well described by $V_{\max} \propto [M_{\text{vir}} E(z)]^\alpha$. In other words, the zero point of the maximum circular velocity evolves with $E(z)^\alpha$. If we adopt the same reasoning, we can assume that the zero point of the Tully-Fisher and Faber-Jackson relations evolve with redshift as $E(z)^{\alpha_{\text{TF}}}$ and $E(z)^{\alpha_{\text{FJ}}}$ respectively, where $\alpha_{\text{TF}} = 0.259$ and $\alpha_{\text{FJ}} = 0.37$ are their corresponding slopes at $z = 0$. The dotted line in Figure 23 shows the predicted cosmic star formation rate density based on this simple evolutionary model. Despite the simplicity of this model, the predictions are much more consistent with observations at high redshifts than the non-evolving model that led to the solid black line in the figure. Nevertheless, the above models are very simple and they ignore the fact that the V_{\max} of dark matter halos is not the $V_{\max,g}$ of galaxies, as we discuss in the next section.

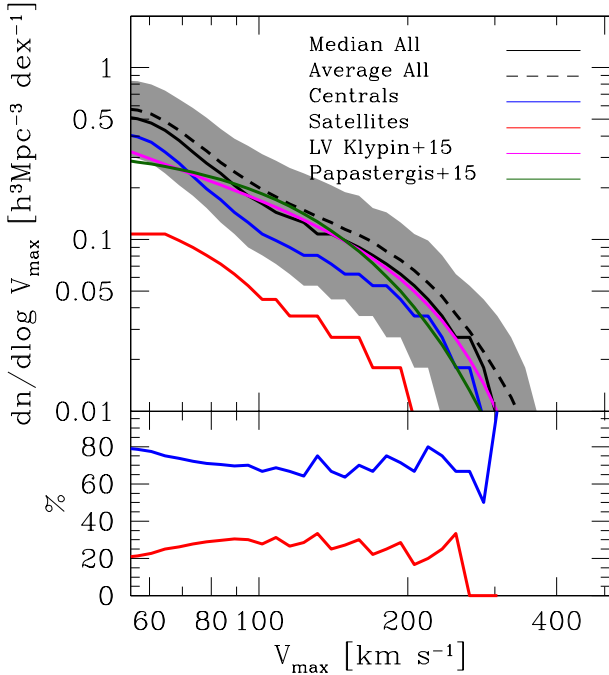


Figure 24. Comparison of the predicted Local Volume 3D velocity function $dN/d\log V$ from the BolshoiP simulation with the observed Local Volume optical velocity function of galaxies within ~ 10 Mpc (Figure 12 of Klypin et al. 2015) and the HI radio velocity function from the ALFALFA survey (Papastergis et al. 2015).

8 OBSERVED VELOCITY FUNCTION OF NEARBY GALAXIES

Previous studies have considered that the observed distribution of galaxy velocities is a strong test for galaxy formation models and cosmology (Cole & Kaiser 1989; Shimasaku 1993; Klypin et al. 1999b). The reason is simply because the comparison, at a first order, between the theoretical halo+subhalo velocity function and the observed velocity function of galaxies is more direct than the stellar mass/luminosity and halo+subhalo mass functions. In this section, we compare the local volume galaxy velocity function derived from optical galaxy observations in Klypin et al. (2015) and the HI radio galaxy velocity function based on the ALFALFA survey from Papastergis et al. (2015) to compare with the theoretical halo+subhalo velocity function from Λ CDM with the Planck cosmological parameters.

In the past, a number of works have studied the velocity function of halos+subhalos from high resolution N-body simulations to conclude that it differs from the observed galaxy velocity function by overpredicting the number of low velocities objects. Actually, these differences are not surprising since a more careful comparison between the theoretical halo+subhalo and galaxy velocity distributions (1) must include the effects of the baryons on the velocity profile of the halo/subhalo, and (2) consistently compare the radii at which galaxies and halo/subhalo velocities (usually V_{\max}) are measured. Indeed, including the effects of the baryons are important since they could increase the maximum circular velocity as a result of their gravitational effect over the halo (but see Dutton et al. 2007).

For item (2) we note that local disk galaxies (which are the most extended objects in the local universe) typically have scale lengths between $R_d \sim 1 - 10$ kpc in the stellar mass range $10^9 - 10^{11.5} M_\odot$. This would imply that V_{\max} of galaxies would be observed between $R(V_{\max}) \sim 2 - 20$ kpc, for the ideal disk $R(V_{\max}) \sim 2.2 \times R_d$. This is actually markedly different from dark matter halos. Assuming that all halos follow a NFW profile, their maximum rotational velocity is reached at $\sim 2.16 \times R_s$. Based on the concentrations obtained in Section 6.1, this would imply that V_{\max} is reached between $R(V_{\max}) \sim 10 - 300$ kpc for halos between $10^{11} - 10^{14} M_\odot$. Clearly using V_{\max} of halos would result in an overestimation of the true maximum circular velocity of the galaxy. Although a more proper modeling of these effects requires sophisticated structural and dynamical models of galaxies like those described in recent papers (Dutton et al. 2007; Trujillo-Gomez et al. 2011; Dutton & van den Bosch 2012; Desmond & Wechsler 2015), in this paper we follow a more empirical approach based on abundance matching. Our goal is to derive a correlation between the maximum circular velocity of galaxies, $V_{\max,g}$, and dark matter halo/subhalos V_{\max} without further modeling of galaxy formation.

We summarize our algorithm as follows:

(i) To each halo/subhalo in the BolshoiP simulation a galaxy with stellar mass M_* is assigned randomly from the probability distribution function $P(M_*|V_{\text{peak}})$. This probability distribution function is assumed to be lognormal with mean $\langle \log M_* \rangle = \langle \log M_* \rangle (\log V_{\text{peak}})$ obtained from abundance matching with halo/subhalo property V_{peak} . The scatter of the distribution is assumed to be constant with V_{peak} with a value of 0.15 dex.

(ii) The next step is to define $P_V(V_{\max,g}|M_*)$ as the log-normal probability distribution that a galaxy of mass M_* has an observed velocity of $V_{\max,g}$. The mean of this distribution, $\langle \log V_{\max,g} \rangle = \langle \log V_{\max,g} \rangle (\log M_*)$, is given by Equation (60). We assume that the scatter of the distribution is constant with M_* with a value of 0.08 dex.

(iii) $V_{\max,g}$ assignment is based on the argument that at a fixed M_* , larger V_{peak} corresponds to larger $V_{\max,g}$. This assumption is reasonable since the halo contributes to the total velocity of the galaxy, $V_{\max,g}$. More formally, we obtain galaxy velocities by solving the following equation for $V_{\max,g}$ for a given M_* :

$$\int_{V_{\max,g}}^{\infty} P_V(V'_{\max,g}|M_*) dV'_{\max,g} = \int_{V_{\text{peak}}}^{\infty} P(V'_{\text{peak}}|M_*) dV'_{\text{peak}}. \quad (61)$$

In the last equation $P(V_{\text{peak}}|M_*)$ is the inverse of the distribution function $P(M_*|V_{\text{peak}})$. A few comments are necessary here: In (i) we use a galaxy stellar mass function that has been corrected for low surface brightness incompleteness in the SDSS and measured over the range between $\log M_*/M_\odot = 10^{7.6} - 10^{12.2}$ (Rodríguez-Puebla et al. in prep). In (ii) we assume that the mean relation given by Equation (60) is valid in the same mass regime. The above procedure ensures that each halo/subhalo in the BolshoiP simulation will host a galaxy with stellar mass M_* and galaxy velocity $V_{\max,g}$. Recall that the BolshoiP simulation is complete for halos with $V_{\max} \gtrsim 50$ km/s.

The Local Volume is a sample of galaxies in a sphere of ~ 10 Mpc centered on the Milky Way. Klypin et al. (2015) showed that the luminosity function of the Local Vol-

ume is consistent with the luminosity function of the local galaxies in the SDSS. This reflects the fact that the Local Volume is not biased to extreme environments such as voids or clusters. In order to define Local Volume analogs in the BolshoiP, we have not carried out an exhaustive search to find similar environments to the Local Volume. Instead, Local Volume analogs are selected by centering spheres of 10 Mpc on galaxies with stellar masses in the bin $\log(M_*/M_\odot) \in [10.64, 10.84]$ corresponding to the mass of the Milky-Way (Flynn et al. 2006), where we have used abundance matching to assign stellar masses to halos in BolshoiP.

The upper panel of Figure 24 shows the predicted velocity function. The black solid line in the figure shows the median velocity function from all the Local Volume analogs found in the simulation, while the dashed curve shows the average. In order to get a sense of the most common configurations of the Local Volume under our definition, we also present the 68% range of the distribution as the grey shaded area. The width of the distribution as a function of mass at low velocities is of the order of ~ 0.25 dex. For comparison, the green solid line shows the fitting function to the observed Local Volume velocity function reported in Klypin et al. (2014). Taking the fairly large dispersion into account, we see that the predicted velocity function is consistent with observations for galaxies above ~ 50 km/s. We also find agreement when comparing with the HI radio galaxy velocity function based on the ALFALFA survey from Papastergis et al. (2015). In the same figure we show predictions of the velocity function decomposed into centrals and satellites. The bottom panel in the same Figure 24 shows the contributions from centrals and satellites. We find that approximately $\sim 80\%$ of the galaxies in the Local Volume are centrals.

9 SUMMARY & DISCUSSION

This paper presents many results, both graphically and with fitting functions, from the Bolshoi-Planck and MultiDark-Planck simulations of the large scale structure of the universe, based on the Planck cosmological parameters summarized in Table 1. Figure 1 shows the WMAP5/7/9 and Planck constraints on the key cosmological parameters σ_8 and Ω_M , and the values adopted for these parameters in many cosmological simulations.

The Bolshoi-Planck and MultiDark-Planck simulations have been analyzed using ROCKSTAR and CONSISTENT TREES to identify and characterize all dark matter halos in all stored time steps, and to construct merger trees of these halos. In this paper we use the virial radius R_{vir} and virial mass M_{vir} , Equation (1), to describe these dark matter halos.

It is useful to characterize dark matter halos by their maximum or peak circular velocity, in addition to their virial mass. Figure 3 shows the relations between V_{max} and M_{vir} and between V_{peak} and M_{vir} . The slopes are roughly given by $V \propto M_{\text{vir}}^{1/3}$, and we give accurate fitting functions in Equation (5).

Cosmological simulations also allow determination of the mass accretion rates of the halos as a function of their virial mass and redshift. Figure 4 shows these accretion

rates three ways: Instantaneous accretion rates (i.e., between stored time steps), accretion rates averaged over the halo's dynamical time, Equation (10), and accretion rates of the maximum mass M_{peak} along the main progenitor branch. We give power-law fitting functions in the form of Equation (11) for all of these, and a better double-power-law fit, Equation (14), for the instantaneous accretion rates.

Rodríguez-Puebla et al. (2016) uses abundance matching with the Bolshoi-Planck simulation to explore the possibility that the halo mass accretion rate plays a large part in determining the star formation rate of the central galaxy in the halo, at least when this galaxy lies on the main sequence of star formation. This Stellar-Halo Accretion Rate Coevolution (SHARC) assumption predicts star formation rates on the main sequence that are in remarkably good agreement with observations for the redshift range $z = 0$ to 4. The paper also shows that the ~ 0.3 dex dispersion in the halo mass accretion rates leads to similar small dispersions in the predicted star formation rates, in rough agreement with observations.

Figures 5 and 6 show the median halo mass growth and the maximum circular velocity growth as redshift decreases, and also the dispersions of these. It is remarkable how little change there is with redshift in the circular velocity of halos of $M_{\text{vir}} = 10^{11} M_\odot$ at low redshifts.

The ROCKSTAR analysis of the Bolshoi-Planck simulation reliably finds all dark matter halos and subhalos with $\gtrsim 100$ particles, which corresponds to $M_{\text{vir}} \gtrsim 2 \times 10^{10} h^{-1} M_\odot$ or $V_{\text{max}} \gtrsim 50$ km/s. All such halos are expected to host visible galaxies, so the number densities of dark matter halos and subhalos as a function of mass and redshift predict the corresponding abundances of central and satellite galaxies. We find that the Tinker et al. (2008) formula Equation (25) is a good approximation to the number density of distinct dark matter halos, shown in Figure 7, and we give a fitting function Equation (29) for the amplitude of fluctuations, shown in Figure 8.

The characteristic mass $M_C(z)$ of 1σ halos just collapsing at redshift z separates abundant halos with $M_{\text{vir}} < M_C$ from relatively rare halos with $M_{\text{vir}} > M_C$. The clustering properties of halos are also different below and above M_C (e.g., Wechsler et al. 2006), and halo properties such as their triaxial shapes scale with M_C (e.g., Allgood et al. 2006). We plot $M_C(z)$ in Figure 9 and give a fitting function Equation (31) for the Bolshoi-Planck cosmological parameters.

The maximum circular velocity of dark matter halos is related to observable internal velocities of their central galaxies or the relative velocities of galaxies in groups and clusters, so it is useful to determine the velocity function of distinct halos. This is plotted in Figure 14, with a corresponding fitting function Equation (41).

The Planck cosmological parameters, especially the higher Ω_M compared with WMAP5/7, result in a greater abundance of halos especially at high masses and redshifts. This is shown in Figure 10. At $z = 0$ there are $\sim 12\%$ more $10^{12} h^{-1} M_\odot$ halos in the Bolshoi-Planck than in the Bolshoi simulation, and $\sim 25\%$ more for $M_{\text{vir}} \sim 3 \times 10^{13} h^{-1} M_\odot$. At $z = 8$ there are about 3 times as many $M_{\text{vir}} = 10^{11} h^{-1} M_\odot$ halos in Bolshoi-Planck as in Bolshoi. Similarly, there are more dark matter halos as a function of V_{max} with the Planck parameters, as shown in Figure 15. At $z = 0$ to 2 there are $\sim 25\%$ more halos with $V_{\text{max}} = 200$ km/s in the

Bolshoi-Planck than in the Bolshoi simulation. This fraction increases at $z = 4, 6$ and 8 , with $\sim 60, 78$ and 258% more $V_{\text{max}} = 200$ km/s halos in the Bolshoi-Planck simulation.

Figure 11 characterizes the abundance of subhalos as a function of the mass they had at accretion, and also as a function of their peak mass along their major progenitor track, with corresponding fitting function given by Equation (35). We also plot the redshift evolution of the subhalo maximum circular velocity at accretion in Figure 16 and the subhalo peak circular velocity function in Figure 17, with fitting functions Equation (43).

It is also useful to know the number of subhalos with a given accreted mass or peak mass compared to the virial mass of the host halo. This is shown in Figure 12, with fitting function Equation (37). It is also useful to know the corresponding numbers of subhalos characterized by their circular velocities. Figure 18 shows the number of subhalos as a function of V_{sub} divided by the maximum circular velocity of the host halo, for V_{sub} equal to the subhalo's velocity at accretion V_{acc} or its peak circular velocity V_{peak} , with fitting function Equation (47).

We calculate the concentration of dark matter halos two ways, by finding the best scale radius R_s assuming a NFW profile or by using Equation (52). Figure 19 shows the resulting concentrations as a function of M_{vir} and redshift from the Bolshoi-Planck, SmallMultiDark-Planck (SMDPL), and MultiDark-Planck (MDPL) simulations.

The halo spin parameter λ is a dimensionless way of characterizing the angular momentum of each dark matter halo. We calculate the halo spin parameter using both the Peebles (1969) definition Equation (54) and the Bullock et al. (2001a) definition Equation (55). The results as a function of M_{vir} and redshift are shown in Figure 20. The value of the Peebles spin parameter λ_P shows a systematic decrease as redshift increases, as was previously noted by Hetzner & Burkert (2006), but λ_B is less dependent on redshift. Since a smaller value of λ is expected to lead to the cooling baryons becoming rotationally supported at a smaller radius, any redshift dependence could have implications for galaxy sizes as a function of redshift. The latest measurements of galaxy size evolution from HST images (Shibuya, Ouchi & Harikane 2015; Curtis-Lake et al. 2014) appear to favor the evolution expected from λ_B .

The Tully-Fisher and Faber-Jackson relations relate rotation velocity V and velocity dispersion σ of galaxies to their stellar masses. When using $V = 1.54\sigma$ and by taking into account the fraction of disk and elliptical galaxies generalize these relations to apply to observed galaxies that have comparable values of V and σ . But Λ CDM simulations show that the cumulative comoving number density of halos with galaxy-scale circular velocities are nearly constant out to rather high redshifts $z \sim 4$ (see Figure 22), while the stellar mass density decreases with increasing redshift. This implies that these stellar mass-velocity relations must change at redshifts $z \gtrsim 1$. In Figure 23 we show this, and also show a simple model of how these relations might change up to redshift $z \sim 9$.

In Section 8 we compare the abundance of dark matter halos with the observed abundance of galaxies in optical and radio surveys. We show that when we take into account effects of baryons on the observed velocities and the effects of the radii where these velocities are measured, and we

compare with the rather wide predicted velocity distribution for volumes of the simulation centered on Milky Way mass galaxies, the agreement between theory and observations is good for low-mass galaxies down to the ~ 50 km/s completeness limit of our simulations, contrary to some claims in the literature.

Λ CDM and observations are also in good agreement at higher masses. There are large catalogs of galaxy cluster observations using X-ray and optical surveys, and recently smaller catalogs of cluster Sunyaev-Zel'dovich detections (Planck Collaboration et al. 2015b). The key to constructing the cluster mass function from these observations is to obtain a reliable mass calibration from gravitational lensing (e.g., Rozo et al. 2014; Mantz et al. 2015). We have shown that the Tinker mass function, Equation (25), is an excellent fit to the abundance of dark matter halos in our simulations, and Mantz et al. (2015); Planck Collaboration et al. (2015b) find that the predicted and observed cluster abundance are in good agreement with the Planck cosmological parameters.

ACKNOWLEDGMENTS

We thank NASA Advanced Supercomputing (NAS) for access to their Pleiades supercomputer where our Bolshoi, MultiDark, and Bolshoi-Planck cosmological simulations were run, and the Leibniz-Rechenzentrum (LRZ) in Munich where the MultiDark-Planck simulations were run on the SuperMUC supercomputer. We also thank the Leibniz Institute for Astrophysics Potsdam (AIP) and the Spanish MultiDark Consolider project for supporting the MultiDark and CosmoSim databases. ARP has been supported by a UC-MEXUS Fellowship. PB was partially supported by a Giacconi Fellowship from the Space Telescope Science Institute (STScI). The remainder of support for PB through program number HST-HF2-51353.001-A was provided by NASA through a Hubble Fellowship grant from STScI, which is operated by the Association of Universities for Research in Astronomy, Incorporated, under NASA contract NAS5-26555. AK, CL, and JP acknowledge support from NSF grant AST-1010033 and the CANDELS grant HST GO-12060 from STScI. We thank Kristin Riebe for giving us permission to use Fig. B1, and we thank Vladimir Avila-Reese, Avishai Dekel, Sandra Faber, Stefan Gottloeber, Susan Kassin, David Koo, Gerard Lemson, Francisco Prada, Joe Silk, Rachel Somerville, and Frank van den Bosch for helpful discussions.

REFERENCES

- Allgood B., Flores R. A., Primack J. R., Kravtsov A. V., Wechsler R. H., Faltenbacher A., Bullock J. S., 2006, MNRAS, 367, 1781
- Angulo R. E., Springel V., White S. D. M., Jenkins A., Baugh C. M., Frenk C. S., 2012, MNRAS, 426, 2046
- Baldry I. K. et al., 2012, MNRAS, 421, 621
- Baldry I. K., Glazebrook K., Driver S. P., 2008, MNRAS, 388, 945
- Behroozi P. S., Wechsler R. H., Conroy C., 2013a, ApJ, 762, L31

- Behroozi P. S., Wechsler R. H., Conroy C., 2013b, *ApJ*, 770, 57
- Behroozi P. S., Wechsler R. H., Wu H.-Y., 2013, *ApJ*, 762, 109
- Behroozi P. S., Wechsler R. H., Wu H.-Y., Busha M. T., Klypin A. A., Primack J. R., 2013, *ApJ*, 763, 18
- Besla G., 2015, *ArXiv e-prints*
- Bett P., Eke V., Frenk C. S., Jenkins A., Helly J., Navarro J., 2007, *MNRAS*, 376, 215
- Bezanson R., van Dokkum P., Franx M., 2012, *ApJ*, 760, 62
- Binney J., Tremaine S., 2008, *Galactic Dynamics: Second Edition*. Princeton University Press
- Blanton M. R., Lupton R. H., Schlegel D. J., Strauss M. A., Brinkmann J., Fukugita M., Loveday J., 2005, *ApJ*, 631, 208
- Boylan-Kolchin M., Springel V., White S. D. M., Jenkins A., 2010, *MNRAS*, 406, 896
- Boylan-Kolchin M., Springel V., White S. D. M., Jenkins A., Lemson G., 2009, *MNRAS*, 398, 1150
- Bryan G. L., Norman M. L., 1998, *ApJ*, 495, 80
- Bullock J. S., Dekel A., Kolatt T. S., Kravtsov A. V., Klypin A. A., Porciani C., Primack J. R., 2001a, *ApJ*, 555, 240
- Bullock J. S., Dekel A., Kolatt T. S., Primack J. R., Somerville R. S., 2001b, *ApJ*, 550, 21
- Busha M. T., Wechsler R. H., Behroozi P. S., Gerke B. F., Klypin A. A., Primack J. R., 2011, *ApJ*, 743, 117
- Cohn J. D., White M., 2005, *Astroparticle Physics*, 24, 316
- Cole S., Kaiser N., 1989, *MNRAS*, 237, 1127
- Conselice C. J., Bundy K., Ellis R. S., Brichmann J., Vogt N. P., Phillips A. C., 2005, *ApJ*, 628, 160
- Covington M. D. et al., 2010, *ApJ*, 710, 279
- Cuesta A. J., Prada F., Klypin A., Moles M., 2008, *MNRAS*, 389, 385
- Curtis-Lake E. et al., 2014, *ArXiv e-prints*
- Dekel A., Birnboim Y., 2006, *MNRAS*, 368, 2
- Desmond H., Wechsler R. H., 2015, *MNRAS*, 454, 322
- Diemand J., Kuhlen M., Madau P., 2007, *ApJ*, 667, 859
- Diemer B., Kravtsov A. V., 2015, *ApJ*, 799, 108
- Diemer B., More S., Kravtsov A. V., 2013, *ApJ*, 766, 25
- Dutton A. A. et al., 2011, *MNRAS*, 416, 322
- Dutton A. A., van den Bosch F. C., 2012, *MNRAS*, 421, 608
- Dutton A. A., van den Bosch F. C., Dekel A., Courteau S., 2007, *ApJ*, 654, 27
- Fakhouri O., Ma C.-P., Boylan-Kolchin M., 2010, *MNRAS*, 406, 2267
- Firmani C., Avila-Reese V., 2013, *MNRAS*, 432, 2420
- Flynn C., Holmberg J., Portinari L., Fuchs B., Jahreiß H., 2006, *MNRAS*, 372, 1149
- Gonzalez A. H., Williams K. A., Bullock J. S., Kolatt T. S., Primack J. R., 2000, *ApJ*, 528, 145
- Hahn O., Porciani C., Dekel A., Carollo C. M., 2009, *MNRAS*, 398, 1742
- Hearin A. P., Watson D. F., van den Bosch F. C., 2015, *MNRAS*, 452, 1958
- Heitmann K. et al., 2015, *ApJS*, 219, 34
- Hetznecker H., Burkert A., 2006, *MNRAS*, 370, 1905
- Hinshaw G. et al., 2013a, *ApJS*, 208, 19
- Hinshaw G. et al., 2013b, *ApJS*, 208, 19
- Hinshaw G. et al., 2009, *ApJS*, 180, 225
- Ishiyama T., Enoki M., Kobayashi M. A. R., Makiya R., Nagashima M., Oogi T., 2015, *PASJ*, 67, 61
- Jarosik N. et al., 2011, *ApJS*, 192, 14
- Jiang F., van den Bosch F. C., 2014, *MNRAS*, 440, 193
- Kassin S. A. et al., 2007, *ApJ*, 660, L35
- Kauffmann G., White S. D. M., 1993, *MNRAS*, 261
- Klypin A., Gottlöber S., Kravtsov A. V., Khokhlov A. M., 1999a, *ApJ*, 516, 530
- Klypin A., Karachentsev I., Makarov D., Nasonova O., 2015, *MNRAS*, 454, 1798
- Klypin A., Kravtsov A. V., Bullock J. S., Primack J. R., 2001, *ApJ*, 554, 903
- Klypin A., Kravtsov A. V., Valenzuela O., Prada F., 1999b, *ApJ*, 522, 82
- Klypin A., Yepes G., Gottlöber S., Prada F., Hess S., 2014, *ArXiv e-prints*
- Klypin A. A., Trujillo-Gomez S., Primack J., 2011, *ApJ*, 740, 102
- Kuhlen M., Vogelsberger M., Angulo R., 2012, *Physics of the Dark Universe*, 1, 50
- Lacey C., Cole S., 1993, *MNRAS*, 262, 627
- Lahav O., Lilje P. B., Primack J. R., Rees M. J., 1991, *MNRAS*, 251, 128
- Lewis A., Challinor A., Lasenby A., 2000, *ApJ*, 538, 473
- Ludlow A. D., Bose S., Angulo R. E., Wang L., Hellwing W. A., Navarro J. F., Cole S., Frenk C. S., 2016, *ArXiv e-prints*
- Ludlow A. D., Navarro J. F., Angulo R. E., Boylan-Kolchin M., Springel V., Frenk C., White S. D. M., 2014, *MNRAS*, 441, 378
- Macciò A. V., Dutton A. A., van den Bosch F. C., Moore B., Potter D., Stadel J., 2007, *MNRAS*, 378, 55
- Madau P., Dickinson M., 2014, *ARAA*, 52, 415
- Mantz A. B. et al., 2015, *MNRAS*, 446, 2205
- McBride J., Fakhouri O., Ma C.-P., 2009, *MNRAS*, 398, 1858
- Mitra S., Davé R., Finlator K., 2015, *MNRAS*, 452, 1184
- Moore B., Ghigna S., Governato F., Lake G., Quinn T., Stadel J., Tozzi P., 1999, *ApJ*, 524, L19
- More S., Diemer B., Kravtsov A., 2015, *ArXiv e-prints*
- Mosleh M., Williams R. J., Franx M., 2013, *ApJ*, 777, 117
- Moster B. P., Naab T., White S. D. M., 2013, *MNRAS*, 428, 3121
- Moster B. P., Somerville R. S., Maubetsch C., van den Bosch F. C., Macciò A. V., Naab T., Oser L., 2010, *ApJ*, 710, 903
- Navarro J. F., Frenk C. S., White S. D. M., 1996, *ApJ*, 462, 563
- Neistein E., Li C., Khochfar S., Weinmann S. M., Shankar F., Boylan-Kolchin M., 2011, *MNRAS*, 416, 1486
- Neistein E., van den Bosch F. C., Dekel A., 2006, *MNRAS*, 372, 933
- Papastergis E., Giovanelli R., Haynes M. P., Shankar F., 2015, *A&A*, 574, A113
- Papastergis E., Martin A. M., Giovanelli R., Haynes M. P., 2011, *ApJ*, 739, 38
- Parkinson H., Cole S., Helly J., 2008, *MNRAS*, 383, 557
- Peebles P. J. E., 1969, *ApJ*, 155, 393
- Planck Collaboration et al., 2014, *A&A*, 571, A16
- Planck Collaboration et al., 2015a, *ArXiv e-prints*
- Planck Collaboration et al., 2015b, *ArXiv e-prints*

Prada F., Klypin A. A., Cuesta A. J., Betancort-Rijo J. E., Primack J., 2012, *MNRAS*, 423, 3018

Prada F., Klypin A. A., Simonneau E., Betancort-Rijo J., Patiri S., Gottlöber S., Sanchez-Conde M. A., 2006, *ApJ*, 645, 1001

Reddick R. M., Wechsler R. H., Tinker J. L., Behroozi P. S., 2013, *ApJ*, 771, 30

Riebe K. et al., 2013, *Astronomische Nachrichten*, 334, 691

Rodríguez-Puebla A., Avila-Reese V., Drory N., 2013a, *ApJ*, 767, 92

Rodríguez-Puebla A., Avila-Reese V., Drory N., 2013b, *ApJ*, 773, 172

Rodríguez-Puebla A., Drory N., Avila-Reese V., 2012, *ApJ*, 756, 2

Rodríguez-Puebla A., Primack J. R., Behroozi P., Faber S. M., 2016, *MNRAS*, 455, 2592

Rozo E., Bartlett J. G., Evrard A. E., Rykoff E. S., 2014, *MNRAS*, 438, 78

Schneider A., Anderhalden D., Macciò A. V., Diemand J., 2014, *MNRAS*, 441, L6

Shibuya T., Ouchi M., Harikane Y., 2015, *ApJS*, 219, 15

Shibuya T., Ouchi M., Kubo M., Harikane Y., 2015, *ArXiv e-prints*

Shimasaku K., 1993, *ApJ*, 413, 59

Skibba R. A. et al., 2015, *ApJ*, 807, 152

Skillman S. W., Warren M. S., Turk M. J., Wechsler R. H., Holz D. E., Sutter P. M., 2014, *ArXiv e-prints*

Somerville R. S., Kolatt T. S., 1999, *MNRAS*, 305, 1

Spergel D. N. et al., 2003, *ApJS*, 148, 175

Springel V. et al., 2005, *Natur*, 435, 629

Srisawat C. et al., 2013, *MNRAS*, 436, 150

Tinker J. L., Conroy C., Norberg P., Patiri S. G., Weinberg D. H., Warren M. S., 2008, *ApJ*, 686, 53

Trujillo-Gomez S., Klypin A., Primack J., Romanowsky A. J., 2011, *ApJ*, 742, 16

Tweed D., Devriendt J., Blaizot J., Colombi S., Slyz A., 2009, *A&A*, 506, 647

van den Bosch F. C., 2002, *MNRAS*, 331, 98

van den Bosch F. C., Jiang F., Hearin A., Campbell D., Watson D., Padmanabhan N., 2014, *MNRAS*, 445, 1713

Watson W. A., Iliev I. T., D’Aloisio A., Knebe A., Shapiro P. R., Yepes G., 2013, *MNRAS*, 433, 1230

Wechsler R. H., Bullock J. S., Primack J. R., Kravtsov A. V., Dekel A., 2002, *ApJ*, 568, 52

Wechsler R. H., Zentner A. R., Bullock J. S., Kravtsov A. V., Allgood B., 2006, *ApJ*, 652, 71

Weiner B. J. et al., 2006, *ApJ*, 653, 1027

Wetzel A. R., Tinker J. L., Conroy C., van den Bosch F. C., 2013, *MNRAS*, 432, 336

Yang X., Mo H. J., van den Bosch F. C., 2009, *ApJ*, 693, 830

Zavala J., Jing Y. P., Faltenbacher A., Yepes G., Hoffman Y., Gottlöber S., Catinaella B., 2009, *ApJ*, 700, 1779

Zehavi I. et al., 2011, *ApJ*, 736, 59

Zehavi I. et al., 2005, *ApJ*, 630, 1

Zhang J., Fakhouri O., Ma C.-P., 2008, *MNRAS*, 389, 1521

APPENDIX A: MERGER TREE OVERVIEW

The publicly available³ ROCKSTAR (Robust Overdensity Calculation using K-Space Topologically Adaptive Refinement) halo finder (Behroozi, Wechsler & Wu 2013) identifies dark matter halos based on adaptive hierarchical refinement of friends-of-friends groups of particles in six phase-space dimensions plus time. For halo masses, ROCKSTAR calculates spherical overdensities using all the particles including any substructures in the halo. Before calculating the halo mass and V_{\max} , the code performs an unbinding procedure using a modified Barnes-Hut method to accurately calculate particle potentials. Behroozi, Wechsler & Wu (2013) describes many halo properties that are calculated by ROCKSTAR, and compares results with the BDM halo finder (Klypin et al. 1999a) that was also used to analyze the Bolshoi simulation (Klypin, Trujillo-Gomez & Primack 2011).

Results from BDM analyses of all the simulations in Table 1 are available online at the CosmoSim website.¹ Those for the ROCKSTAR analyses of the Bolshoi-Planck, SMDPL, and MDPL simulations can be downloaded in bulk from the UCSC Hyades system.² Complete particle data was saved for 178 timesteps of the Bolshoi-Planck simulation, 117 timesteps of SMDPL, and 126 timesteps of MDPL. For scale factor $a = 0.06 - 0.09$ the scale factor change between timesteps was $\Delta a \sim 0.0021$, for $a = 0.09 - 0.14$ $\Delta a \sim 0.0035$, for $a = 0.14 - 0.7$ $\Delta a \sim 0.005$, and for $a = 0.7 - 1$ $\Delta a = 0.007$. Thus the time interval between stored timesteps ranges from ~ 10 Myr at $z \sim 15$ to ~ 100 Myr at $z = 0$. The cadence of these timesteps is shown in Figure A1.

CONSISTENT TREES (Behroozi et al. 2013) generates merger trees and halo catalogs in a way that ensures consistency of halo mass, position, and velocity across time steps. This allows it to repair inconsistencies in halo catalogs—e.g., when a halo disappears for a few time steps, CONSISTENT TREES can regenerate its expected properties by gravitational evolution from the surrounding time steps. The CONSISTENT TREES code is publicly available,⁴ and CONSISTENT TREES outputs used in this paper are available online.² In these Appendixes we describe how these outputs are organized.

CONSISTENT TREES generates merger tree information in **tree files** (`tree_*.dat`), which each contain halos and their full progenitor histories for cubical subvolumes of the simulation. It also generates **catalogs** (`hlist_*.list`), which each contain all the halos for a single snapshot of the simulation, along with frequently-used information from their merger histories (e.g., peak mass, half-mass assembly time, mass accretion rate, etc.). These enable the user to avoid walking the trees for many common applications (e.g., abundance matching).

A1 Tree File Layout

Tree files contain header information (lines beginning with a `#` character), a single line with the total number of trees in the file, and then the actual merger trees. Each merger tree corresponds to the progenitor history of a single halo at

³ <http://code.google.com/p/rockstar>

⁴ <https://bitbucket.org/pbehroozi/consistent-trees>

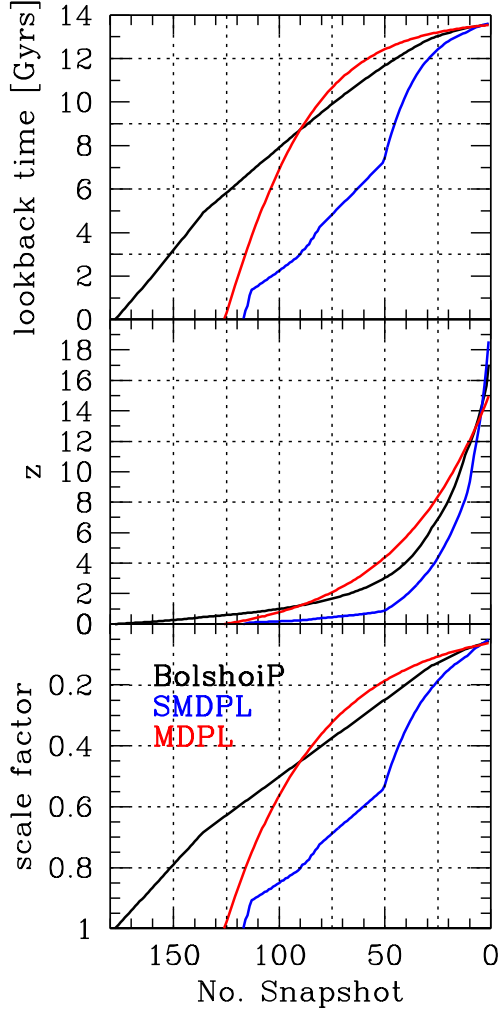


Figure A1. Lookback time, redshift, and scale factor vs. snapshot number for the BolshoiP, SMDPL, and MDPL simulations. Many high redshift timesteps were saved in order to be able to construct merger trees for halos forming at high redshifts.

the last snapshot of the simulation, containing all halos that fully merge (a.k.a., are disrupted) into the final halo. Specifically, subhalos that remain distinguishable from their host halo at the last simulation snapshot have separate merger trees in the tree files. Each tree file contains the merger histories for halos whose centers lie in a cubical subvolume of the simulation. For example, the Bolshoi simulation has 125 ($=5 \times 5 \times 5$) tree files, each corresponding to a $(50 \text{ Mpc}/h)^3$ subvolume of the total $(250 \text{ Mpc}/h)^3$ simulation volume.

The merger trees' basic format is a single header line with the final halo's ID (**#tree XYZ**), also known as the **tree root ID**, followed by single lines for each halo in the full merger history, ordered by snapshot:

```
#tree XYZ
halo XYZ @ snapshot N
progenitor 1 @ snapshot N-1
progenitor 2 @ snapshot N-1
...
progenitor P @ snapshot N-1
progenitor 1 @ snapshot N-2
```

```
...
progenitor Q @ snapshot N-2
...
progenitor 1 @ snapshot 1
...
progenitor Z @ snapshot 1
```

The format of the halo lines is described in Appendix B. Note here that the order of progenitors within a snapshot is not guaranteed; also, progenitors may not exist at all snapshots, especially if the final halo is close to the mass resolution of the simulation. Flyby halos (i.e., halos that pass in and out of the virial radius of a host, also called spashback halos) are similarly not guaranteed to be included in the merger history.

For some applications (e.g., semi-analytic models, SAMs), it is necessary to process merger histories including all flyby halos and subhalos. These are also known as **forests**. CONSISTENT TREES provides a **forests.list** file; each line of the file contains a tree root ID and the corresponding forest ID. All merger trees with the same forest ID belong to the same forest. To aid with collating forests from the tree files, CONSISTENT TREES also provides a **locations.dat** file; each line of the file contains a tree root ID, a tree filename, and the byte offset in the tree file at which the given merger tree may be found.

A2 Catalog File Layout

Catalog files (**hlist*.list**) contain all the halos at a given snapshot of the simulation. The number in the filename corresponds to the scale factor a ; e.g., **hlist_1.00000.list** corresponds to the simulation output at $a = 1.0$. These files contain header information (lines beginning with a **#** character), followed by a single line for each halo in the given snapshot. The halo line format follows that of the tree files, but includes several additional fields at the end. All fields are described in Appendix B.

A3 Alternate Formats

The above two formats are the only ones generated by default. Converters also exist for the SUSSING, GALACTICUS, and IRATE formats; please contact Peter Behroozi (pbehroozi@gmail.com) for details.

APPENDIX B: MERGER TREE FIELDS

Each halo line contains several fields separated by a space character (" "), giving information about the halo's identification, properties, order within the merger tree, and so on. Please note that the ordering of some fields may change in new versions of CONSISTENT TREES. However, the first header line in both the tree files and the catalogs always lists the field order, so it is always a good idea to *double-check this line* with what your code is expecting.

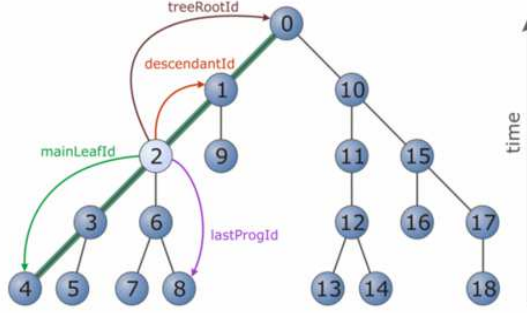


Figure B1. Illustration of a merger tree. The top node (root) of the tree represents a halo at a given redshift. From there, branches reach backwards in time to its progenitors, i.e., the timeline goes from bottom to top. The numbers at each node indicate the depth-first order, with the most massive progenitors being on the leftmost side of each sub-tree. These form the main branch (e.g., the thick green line for the tree root (0)) of the corresponding node. (Used with permission from Riebe et al. (2013); figure ©2013 WILEY-VCH Verlag GmbH & Co. KGaA, Weinheim.)

B1 Halo Identification and Properties

The following fields are always guaranteed to exist, and will always exist in the following order at the beginning of the line:

- Scale: Halo’s scale factor.
- ID: Halo ID, guaranteed to be unique across all snapshots of the entire simulation. Because CONSISTENT TREES adds and deletes halos, this may be different from the ID returned by the halo finder.
- Desc_Scale: Scale factor of descendent halo, if applicable.
- Descid: Halo ID of descendent halo, if applicable.
- Num_prog: Number of progenitor halos—i.e., number of halos at the immediately preceding snapshot that fully merge into this halo.
- Pid: Parent halo ID. For distinct halos (those that are not subhalos), this is -1. Otherwise, it is the halo ID of the smallest host halo (ordered by V_{max}) that contains this halo’s center within its radius.
- Upid: Über-parent halo ID. For distinct halos, this is -1. Otherwise, it is the halo ID of the largest host halo (ordered by V_{max}) that contains this halo’s center within its radius. Note that it is geometrically possible for a subhalo to be within the virial radius of more than one distinct halo. Hence, there is no guarantee that the parent halo is a subhalo of the über-parent halo if the two IDs are different.
- Phantom: Zero (i.e., ignorable) for most halos. This is nonzero only when the halo finder did not return an appropriate progenitor halo at this snapshot and CONSISTENT TREES had to interpolate halo properties from nearby snapshots.
- SAM_Mvir: *Do not use*. For historical reasons, this was needed by certain semi-analytical models.
- Mvir: Halo mass, in units of M_{\odot}/h .
- Rvir: Halo radius, in units of comoving kpc/ h .
- Rs: NFW scale radius, in units of comoving kpc/ h .
- Vrms: Halo particle velocity dispersion, in units of physical (i.e., non-comoving) km/s.
- mmp?: 1 if the halo is the most-massive progenitor of its descendent halo; 0 if not.
- scale_of_last_MM: scale factor of the halo’s last major merger. This is typically defined as a mass ratio greater than

0.3:1, although it is user-adjustable. The exact definition always appears in the header lines.

- Vmax: Maximum halo circular velocity (i.e., maximum of $\sqrt{GM(< R)/R}$, where $M(< R)$ is the mass enclosed within radius R), in units of physical km/s.
- X/Y/Z: Halo position, in units of comoving Mpc/ h .
- VX/VY/VZ: Halo velocity, in units of physical km/s.
- JX/JY/JZ: Halo angular momentum, in units of $(M_{\odot}/h) \times (\text{Mpc}/h) \times \text{km/s}$ (physical).
- Spin: Dimensionless halo spin parameter. (Peebles spin, Equation (54), for ROCKSTAR).

B2 Halo Ordering, Cross-Referencing, and Tree Walking

When walking trees, there are two main approaches. The first is *breadth-first*, in which halos are ordered and accessed according to the simulation snapshot; this is the default halo ordering in the trees. An alternate method is *depth-first*, in which halos are ordered and accessed first along main progenitor branches (i.e., following the most-massive progenitor line) followed by the next-most-massive progenitor branches. For an illustration, see Figure B1.

The following fields will always exist in current and later versions of CONSISTENT TREES, although more ordering fields may be added at a later date:

- Breadth_first_ID: Unique ID (across all simulation snapshots) corresponding to the breadth-first order of halos within a tree. Sorting on this ID always recovers the original order in which the halos were printed in the tree file.
- Depth_first_ID: Unique ID (across all simulation snapshots) corresponding to the depth-first ordering of halos within a tree. Sorting on this ID reorganizes the tree into depth-first order. This ordering has the useful property that full merger histories are contiguous, even for halos not at the last simulation snapshot; see Last_progenitor_depthfirst_ID and Last_mainleaf_depthfirst_ID below.
- Tree_root_ID: Halo ID of the final descendent halo (i.e., the descendent halo at the last simulation snapshot).
- Orig_halo_ID: Original halo ID from halo finder, except for phantom halos. This allows cross-referencing halos in the merger trees with other data (e.g., particles) saved by the halo finder.

- **Snap_num**: Snapshot number from which the halo originated—necessary as not all halo finders generate unique IDs.

- **Next_coprogenitor_depthfirst_ID**: Depth-first ID of next “coprogenitor”—i.e., the next halo that shares the same descendent halo.

- **Last_progenitor_depthfirst_ID**: Depth-first ID of last progenitor. When a merger tree is sorted by depth-first ID, then the halos between this halo’s **Depth_first_ID** and this halo’s **Last_progenitor_depthfirst_ID** correspond to its full merger history.

- **Last_mainleaf_depthfirst_ID**: Depth-first ID of last progenitor on this halo’s main progenitor branch. When a merger tree is sorted by depth-first ID, then the halos between this halo’s **Depth_first_ID** and this halo’s **Last_mainleaf_depthfirst_ID** correspond to its most-massive progenitor history.

Note that to better understand the last two fields, it is helpful to refer to Figure B1.

B3 Additional Halo Properties

These fields are halo-finder dependent. With the current version of CONSISTENT TREES and ROCKSTAR, they include:

- **Tidal_Force**: Strongest tidal force from any nearby halo, in dimensionless units ($R_{\text{halo}}/R_{\text{hill}}$). The Hill radius (see, e.g., Hahn et al. 2009; Hearin, Watson & van den Bosch 2015) is an upper bound on the spatial extent of newly infalling material that can remain gravitationally bound to a secondary halo. It is given by $R_{\text{hill}} = D(M_{\text{sec}}/3M_{\text{prim}})^{1/3} = R_{\text{sec}}(D/3^{1/3}R_{\text{prim}})$, where the primary (secondary) halo is the larger-virial-radius (smaller-virial-radius) halo of a pair whose centers are separated by distance D .

- **Tidal_ID**: Halo ID of halo exerting strongest tidal force.

- **Rs_Klypin**: NFW scale radius in units of comoving kpc/ h , determined using V_{max} and M_{vir} , Equation (52).

- **Mvir_all**: Halo mass, including unbound particles (M_{\odot}/h).

- **M200m–M2500c**: Mass (M_{\odot}/h) enclosed within specified overdensities. These include 200m, 200c, 500c, and 2500c, where ρ_c is critical density and $\rho_m = \Omega_M \rho_c$ is the mean matter density.

- **Xoff**: Offset of halo center (defined as the density peak) from the center of mass within the halo radius (comoving kpc/ h).

- **Voff**: Offset of halo center (defined as the density peak) from average particle velocity (physical km/s).

- **Spin_Bullock**: Bullock spin parameter, Equation (55).

- **b_to_a, c_to_a**: Ratio of second and third largest shape ellipsoid axes (B and C) to largest shape ellipsoid axis (A) (dimensionless), calculated according to the method in Allgood et al. (2006). Additional subscripts (e.g., 500c) indicate that only particles within a specified halo radius are considered.

- **A[x], A[y], A[z]**: Largest shape ellipsoid axis (comoving kpc/ h). Additional subscripts (e.g., 500c) indicate that only particles within a specified halo radius are considered.

- **T/|U|**: ratio of kinetic to potential energies for halo particles.

- **M_pe_***: Pseudo-evolution corrected masses (very experimental).

B4 Additional Catalog Fields

These fields are not in the trees, but are provided for convenience in the halo catalogs. Their order and content may change in future CONSISTENT TREES versions.

- **$M_{\text{acc}}, V_{\text{acc}}$** : Halo’s (or its main progenitor’s) mass and V_{max} at the last timestep that it was a distinct halo.

- **$M_{\text{peak}}, V_{\text{peak}}$** : Peak mass and peak V_{max} along the halo’s main progenitor branch.

- **Halfmass_Scale**: Scale factor at which the halo mass in the main progenitor branch first reaches half of M_{peak} .

- **Acc_Rate_***: Halo mass accretion rates in $M_{\odot}/h/\text{yr}$. These include: *Inst* (averaged since the previous snapshot); *100Myr* (averaged over past 100 Myr); *X*Tdyn*: averaged over past X virial dynamical times (i.e., $X/\sqrt{G\rho_{\text{vir}}}$); *Mpeak*: averaged growth of M_{peak} , averaged from the current halo’s redshift (z) to $z + 0.5$.

- **Mpeak_Scale**: Scale at which M_{peak} was reached along the main progenitor branch.

- **Acc_Scale**: Last scale at which the halo (or its main progenitor) was distinct.

- **First_Acc_Scale**: Last scale at which the halo (or its main progenitor) and all earlier progenitor halos were all distinct.⁵

- **First_Acc_(Mvir|Vmax)**: M_{vir} and V_{max} at **First_Acc_Scale** for the main progenitor.

- **Vmax@Mpeak**: Main progenitor’s V_{max} at **Mpeak_Scale**.

- **Tidal_Force_Tdyn**: Dimensionless tidal force averaged over the past virial dynamical time.

⁵ In theory. In practice, flybys often happen for very early progenitors, so these are ignored if halos at least double their mass following the flyby.